

https://dspace.org/

Characteristics and use of a high resolution E-E gas-ionisation detector for nuclear particle identification

Jingo, Maxwell

2010-08-04
http://hdl.handle.net/10539/8360

Downloaded from a DSpace repository. https://dspace.org/

CHARACTERISTICS AND USE OF A HIGH RESOLUTION Δ*E*-*E* GAS-IONISATION DETECTOR FOR NUCLEAR PARTICLE IDENTIFICATION

Maxwell Jingo

A Research Report submitted to the Faculty of Science, University of the Witwatersrand, Johannesburg, in partial fulfilment of the requirements for the degree of Master of Science

Johannesburg, 2010

Declaration

I declare that this Research Report is my own, unaided work. It is being submitted for the partial fulfilment of the requirements for the degree of Master of Science in the University of the Witwatersrand, Johannesburg. It has not been submitted before for any degree or examination in any other University.

Signature: 

Student name: Maxwell Jingo

Date: 07 June, 2010.

Abstract

Certain particle identification detectors operate on the principle of energy loss. The Δ*E*-*E* gas-ionisation telescope is a good example of such a detector, where incident ions traverse the Δ*E* gas-ionisation cavity of the detector and stop in a solid-state silicon surface-barrier *E* detector. Signals from the detectors are amplified and, if they meet certain time coincidence and amplitude criteria they are added together to provide the total ion energy. From the previous study done at iThemba LABS (Gauteng), a gas mixture of argon and methane was used, but in this particular study, iso-butane was used and new Δ*E* detector operating conditions were determined. Furthermore, an elastic-scattering angular distribution for the scattering reaction of $^{16}O + ^{28}Si$ was also obtained by bombarding an evaporated self-supporting SiO_2 target with a heavy-ion beam of ^{16}O at an incident energy of 30.000 ± 0.038 MeV. The scattered ^{16}O particles were detected by the Δ*E*-*E* gas-ionisation detector and the CAMAC + WIMPS2 data acquisition system was used to identify the particles on-line. The present data are consistent with those obtained previously using the same system for an incident beam energy of 32 MeV. In addition, the reliability and integrity of the refurbished EN Tandem accelerator and beam line (C-line) has been demonstrated.

Dedication

This work is dedicated to Praise Nkosikhona Jingo.

Acknowledgements

I am grateful to iThemba LABS (Gauteng) and the University of the Witwatersrand for their financial support. I would like to thank my supervisor, Prof J. Carter and co-supervisor, Prof E. Sideras-Haddad for their assistance in the data analysis and guidance in writing up of the Research Report, iThemba LABS (Gauteng) Junior Scientists, Dr M. Madhuku, Mr K. Sekhonya for their guidance in the use of ORIGIN Programme, technicians at iThemba LABS (Gauteng) namely Mr Oleg Pekar and Fritz Balzun, for their assistance in the running of the Nuclear Physics Experiments as well as my colleagues, Mr C.O. Kureba and Ms I. Usman, for their discussions concerning this Report. I would also like to thank the librarian, Ms D. Mahlare, iThemba LABS (Gauteng) Secretary, Ms D. Monyamane and lastly but not least Ms N. Radebe for their unwavering and overwhelming support during my period of study.

Table of Contents

Contents **Page**

Declaration.....(ii)

Abstract.....(iii)

Dedication.....(iv)

Acknowledgements.....(v)

List of Figures.....(viii)

List of Tables.....(ix)

Chapter 1 - Introduction.....1

1.1 Purpose and Structure of Study.....2

Chapter 2 - Theoretical Considerations.....4

2.1 Theory of operation of a gridded parallel-plate ionisation detector.....4

2.2 Heavy-ion elastic scattering.....9

2.2.1 Rutherford scattering.....10

2.2.2 Schrödinger Equation for scattering.....11

2.2.3 The optical model of heavy-ion elastic scattering.....13

Chapter 3 - C-line and the Δ*E*-*E* gas-ionisation detector.....17

3.1 Newly refurbished C-line.....17

3.2 Alignment of the C-line.....19

3.3 Δ*E*-*E* gas-ionisation detector gas delivery system.....20

3.3.1 Iso-butane gas delivery system.....23

3.3.2 Iso-butane gas cylinder.....23

3.4 Optimisation and Testing of the EN Tandem accelerator.....27

3.5 Characteristics of the Δ*E*-*E* gas-ionisation detector.....29

3.6 Heavy-ion scattering measurement using the

Δ*E*-*E* gas-ionisation detector.....34

3.6.1 Beam production and transportation.....36

3.7 Data Acquisition System.....37

Chapter 4 - Measurement of $^{16}O + ^{28}Si$ elastic scattering: data extraction, analysis and discussion.....39

4.1.1 Energy resolution of Δ*E*-*E* gas-ionisation detector.....40

4.1.2 Treatment of Errors……....42
4.2 Determination of scattering cross-sections…….....43
4.3 Analysis for elastic scattering of $^{16}O + ^{28}Si$…….....43
4.4 Optical model analysis of $^{16}O + ^{28}Si$…….....45
4.4.1 Woods-Saxon Potential.....45
4.5 Discussion…….....46
Chapter 5 - Conclusions…….....47
Bibliography…….....48
Appendix-Tabulated values of the measured Quantities…….....51

List of Figures

Figure 2.1: Electrodes in a gridded parallel-plate ionisation detector…….....7

Figure 2.2: The dependence of charge losses to the grid on the ratio of the field strengths..…….....8

Figure 2.3: Path followed by a charged particle undergoing Rutherford scattering.....11

Figure 3.1: The schematic diagram for the C-line and associated equipment at the EN Tandem accelerator of iThemba LABS (Gauteng).....18

Figure 3.2: A schematic diagram of the Δ*E*-*E* gas-ionisation gas delivery system.…….....21

Figure 3.3: Photograph of the Δ*E*-*E* gas-ionisation gas delivery system and beam line components…….....22

Figure 3.4: Photograph of the Δ*E*-*E* gas-ionisation gas delivery system and associated valves.....24

Figure 3.5: The extracted negative ions after an inflection magnet scan of an 860 C sputter ion source employing a graphite target…….....28

Figure 3.6: Schematic diagram of the Δ*E*-*E* gas-ionisation detector …….....29

Figure 3.7: The dependence of the Δ*E* maximum peak on the potential difference between the grid and the cathode….....32

Figure 3.8: The dependence of the Δ*E* maximum peak on the potential difference between the anode and the grid....….....33

Figure 3.9: Block diagram of the electronics associated with the Δ*E*-*E* gas-ionisation detector…….....38

Figure 3.10: Two-dimensional Δ*E*-E_{T} spectrum of ^{16}O on ^{28}Si at E_{Lab} = 30.000 ± 0.038 MeV and θ_{Lab} = 20.5°.…….....41

Figure 3.11: One-dimensional Δ*E*-E_{T} spectrum of ^{16}O on ^{28}Si at E_{Lab} = 30.000 ± 0.038 MeV….....42

Figure 3.12: Angular distribution for elastic scattering of $^{16}O + ^{28}Si$ at $E_{Lab} = 30.000 \pm 0.038$ MeV……44

List of Tables

Table 3.1: Safety checks before starting up the Δ*E*-*E* gas-ionisation detector gas delivery system.....25

Table 3.2: Δ*E*-*E* gas-ionisation detector gas delivery system shutting down procedure.....25

Table 3.3: Δ*E*-*E* gas-ionisation detector gas delivery system starting up procedure.....26

Table 3.4: Best operating conditions for the Δ*E* gas-ionisation detector determined using iso-butane gas at a differential pressure of 1 kPa.....31

Table 3.5: Scattering angles covered in $^{16}O + ^{28}Si$ measurements.....35

Table 3.6: Parameters that were used to calculate the Coulomb barrier energy.....35

Table 3.7: Parameters that were used to produce an $^{16}O^{5+}$ beam of 30.000 ± 0.038 MeV.....36

Table 3.8: Optical potential parameters used in the optical model calculations.....46

Chapter 1

Introduction

The 6 MV EN Tandem accelerator at the Schonland Research Institute for Nuclear Sciences since being commissioned in the early 1970's was the property of the University of the Witwatersrand. It was donated to the Department of Science and Technology (DST) as a national facility administered by the National Research Foundation (NRF) and run by iThemba LABS (iTL) in December 2004. The accelerator was refurbished with the aim to meet the stringent needs of today's nuclear physics studies. The following sections were refurbished; the negative-ion source was redesigned and upgraded to an 860 C sputter source, while on the accelerator side, the belt charging system was replaced with a pelletron charging system, new axial electric and spiralled magnetic field tubes were installed, the gas stripper was converted to a recirculation type with a high-voltage terminal pumping system, new high-voltage grading resistors and resistor mounts were installed, and then looking at the control system, a new centralised computer control system and customised software was developed and put into operation [LA07].

Now with the advent of high-quality, stable and light heavy-ion beams, the programme of nuclear structure studies, already started in the 1970's, can continue. The previously used 30° E beam line (now the C-line) is back in operation and incorporates a large scattering chamber (30″ diameter) used typically with an array of silicon surface-barrier detectors followed by a small scattering chamber incorporating a high resolution ΔE-E gas-ionisation detector. The detector makes use of the ΔE-E technique, which has proven to be a very powerful tool for the identification of nuclear particles [BA75]. Charged particles identified in the ΔE-E technique range from light ions to heavy ions. The use of high resolution ΔE-E gas-ionisation detectors has taken over ΔE-E silicon detectors because of their ability to withstand radiation damage and the difficulties associated with fabricating totally depleted thin silicon detectors for the ΔE part. However, in the event of a silicon surface-barrier detector being used for the ΔE part of the present detector, its

equivalent thickness at a differential pressure of 1 kPa using iso-butane gas would be impossibly thin at only 2.85 µm. The manipulation of the Δ*E* and *E* signals involves employing the Δ*E*.*E* 'multiplier' algorithm based on the Bethe-Bloch equation to generate a parameter whose value is characteristic of a specific type of ion [LI37]. In this research work, on-line identification of the Δ*E* and *E* signals was achieved by the use of CAMAC + WIMPS2 data acquisition system [FE92].

1.1 Purpose and Structure of this Study

The previous operating conditions for the Δ*E*-*E* gas-ionisation detector were described in [CA81], now there is need to obtain new operating conditions having changed over the gas used in the Δ*E* part from a mixture of argon and methane, in the ratio of 9:1, to iso-butane gas of chemical purity. The new gas has a better energy deposition characteristic and, therefore produces strong ion signals due to higher energy loss per unit pressure in iso-butane gas [AD06], [JA83]. The absence of leaks on the Δ*E*-*E* gas-ionisation gas delivery system facilitates the attainment of largest energy loss signals during the experimental work since oxygen from the atmosphere causes signal losses.

Furthermore, the presence of the OXISORB filter (final purity: O_2 < 5 ppb and H_2O < 30 ppb) minimises additional oxygen and moisture contamination from the iso-butane gas bottle by two processes known as *chemisorptions* and *physisorption* respectively. In *chemisorptions*, oxygen is chemically bound to the absorption material (e.g. silica gel with chromium) and is, therefore, permanently removed from the gas flow. On the other hand, moisture will be removed by *physisorption*, where the moisture will be physically bound to the silica gel (absorption material) and is, therefore, again removed from the gas flow. In addition, the gas delivery system has been rebuilt to incorporate an electronic pressure control system and gas flow regulator. Operational requirements require ± 5% stability at a differential pressure of 1 kPa.

Once commissioned and as a check for the reliability of the system and associated electronics the Δ*E*-*E* gas-ionisation detector was used to measure ^{16}O + ^{28}Si elastic

scattering at E_{Lab} = 30.000 ± 0.038 MeV in order to obtain and compare data with a study already completed at a nearby incident energy of E_{Lab} = 32 MeV [CA78].

The elastic scattering cross-sections for $^{16}O + ^{28}Si$ obtained experimentally can be normalised to the Rutherford scattering cross-sections at the smaller scattering angles and the angular distribution obtained can be compared to an optical model prediction which includes nuclear effects at the larger scattering angles.

The layout of this Research Report is as follows:

- Chapter 2 presents a description of the theory of operation of a gridded parallel-plate ionisation detector, Rutherford scattering, details of the Schrödinger equation for scattering and its application to the optical model of elastic scattering which will be used to analyse the experimental scattering data.

- Chapter 3 presents a description of the newly refurbished C-line and its alignment, use of the Δ*E*-*E* gas-ionisation gas delivery system, the procedures which were followed during the use of the Δ*E*-*E* gas-ionisation gas delivery system, characteristics of the Δ*E*-*E* gas-ionisation detector, details of the optimisation and testing procedure of the EN Tandem accelerator, the use of the Δ*E*-*E* gas-ionisation detector in measurements involving heavy-ion scattering, beam details and details of the data acquisition system.

- Chapter 4 presents the $^{16}O + ^{28}Si$ elastic scattering: data extraction procedure that was followed, energy resolution of the Δ*E*-*E* gas-ionisation detector system, treatment of errors and determination of the elastic scattering cross-sections. Finally, the analysis of the elastic scattering cross-sections using the optical model prediction is presented.

- Chapter 5 presents the conclusions.

Chapter 2

Theoretical Considerations

Reactions involving the bombardment of target nuclei by high-velocity nuclear projectiles at and above the Coulomb barrier produced by accelerators such as cyclotrons and tandem accelerators have since the inception of such accelerators provided an important probe of nuclear structure. Such nuclear structure studies leading to more complex nuclear reactions produce many reaction products.

For example, in the earliest experiments the bombardment of a ^{12}C target by 24 MeV deuterons produced the reactions $^{12}C(d, \alpha)^{10}B$, $^{12}C\,(d, t)^{11}C$, and $^{12}C(d, d)^{12}C$ (elastic scattering) [GO64]. The energy of the emitted particle is in each case, determined by the energy level of the final nucleus, since the final nucleus can be produced in a series of excited states (or in its ground state). The spectrum from the emitted particles, corresponding to only one of the above reactions, consists of a series of peaks covering a wide energy range. Consequently, the measurement of spectra of the emitted reaction particles has proved to be an effective tool in the study of nuclear energy levels. Thus, the interpretation problem of complex spectra which may sometimes be quite difficult has been solved by the use of a reliable detection system which should not only measure the energy of a particle but also identifies it. A high resolution ΔE-E gas-ionisation detector is one good example of such a detection system that is capable of handling many different nuclear reactions.

2.1 Theory of operation of a gridded parallel-plate ionisation detector

In order to identify the scattered reaction products and determine kinematic energies a suitable method is required. One of the commonly used technique for particle identification is the ΔE-E method which employs a detector telescope for measuring the energy loss, ΔE, of a particle passing through a thin detector into a thick detector where its residual energy, E', is deposited and measured. The total energy, $E_{T,}$ is obtained by summing the ΔE and E' signals:

$$E_T = \Delta E + E'. \tag{2.1}$$

In the case of a thin gas-ionisation ΔE detector, the rate of energy loss by ionisation along the particle's track is given by the Bethe-Bloch equation [GO64]:

$$\frac{dE}{dx} = \frac{4\pi q^4 Z^2}{mV^2} Nz \left[\ln \frac{2mV^2}{I} - \ln\left(1-\beta^2\right) - \beta^2 \right], \tag{2.2}$$

where

$\frac{dE}{dx}$ = rate of energy loss of the particle,

q, m = charge and mass of the electron,

Z, V = atomic number and velocity of the particle,

z = atomic number of the absorber,

N = number of atoms per cc of the absorber,

β = particle velocity/velocity of light and

I = average energy to ionise atoms of the absorber.

If $\beta \ll 1$, Eq. (2.2) simplifies to

$$\frac{dE}{dx} = K_1 \frac{MZ^2}{E} \ln K_2 \frac{E}{M}, \tag{2.3}$$

where K_1 and K_2 are constant and E, M and Z are the energy, mass and atomic number of the particle, respectively.

Since the logarithmic term is not a sensitive function of energy, Eq. (2.3) is usually further approximated to give

$$\left(\frac{dE}{dx}\right) E = K_3 M Z^2. \tag{2.4}$$

Equation (2.4) forms the basis for many particle identifiers, since signals obtained from a thin ΔE detector and from a thick E' detector can be multiplied together to

give the left-hand side of Eq. (2.4), which in turn determines the value of MZ^2 and, therefore, identifies the particle.

However, in this study a high resolution ΔE-E gas-ionisation detector which uses a similar technique as the above mentioned was used. In this particular detector, scattered particles ions pass through a gas-filled space and come to rest in a solid-state silicon surface-barrier detector. The charged particles lose some energy, ΔE, as they pass through the gas, due to ionisation of gas molecules.

Recognition of light ions such as protons, deuterons, tritons, ^{3}He and ^{4}He ions has been observed to be easy since the relative change in energy loss between successive isotopes is quite large. However, an attempt to identify heavier ions has proved to be a difficult task because the energy losses of adjacent ions are quite close to each other, thus in order to identify these ions, some additional time-of-flight measurements may be required [GO79].

A two-electrode parallel-plate ionisation detector such as a ΔE-E gas-ionisation detector has an inherent disadvantage in that its output pulse height normally depends on the position of the initial ionisation event and the motion of the positive ions [WI50a]. This so-called position-ion effect can be eliminated by the introduction of a third electrode between the plates which plays an important role of screening the collector electrically from the entire volume in which the particle tracks are formed.

The standard method employs a Frisch grid as shown in Fig. 2.1. In the absence of the grid electrode, $c = 0$ and formation of an ion pair at P in Fig. 2.1, the charge induced by the positive ion, +e, on the anode becomes:

$$Q = -e\{1-(b/a)\}. \tag{2.5}$$

The role played by the Frisch grid is to shield the anode from the effects of the positive ion since some of the lines of the force from the charge end on the grid instead of on the anode. The charge induced by the positive ion can then be written as:

$$Q = -\sigma e\{1-(b/a)\}, \tag{2.6}$$

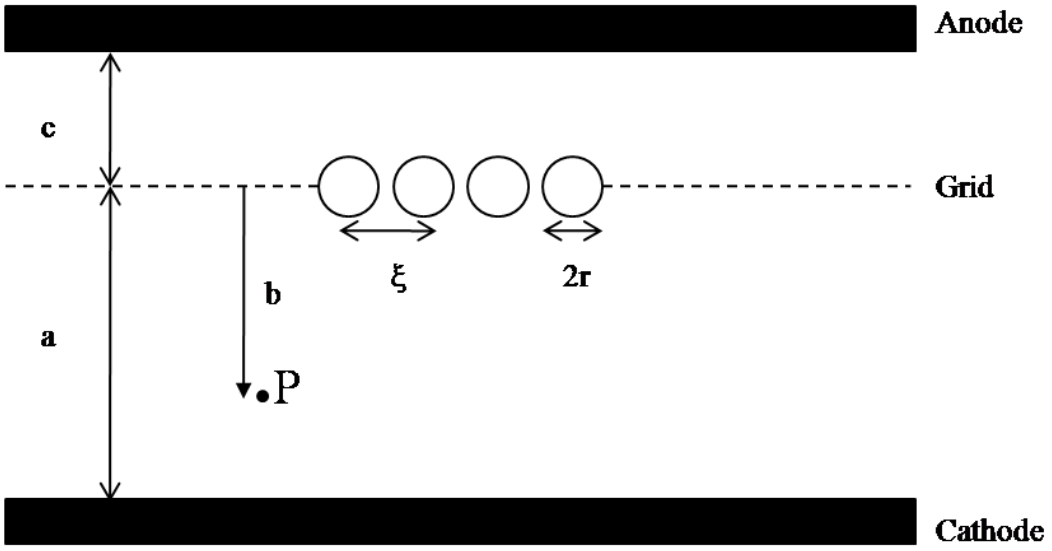

Figure 2.1: Electrodes in a gridded parallel-plate ionisation detector.

where σ is a parameter known as the shielding inefficiency of the grid [BU46].

The parameter σ is a measure of the degree of shielding provided by the grid and its value depends on the geometry of the grid. For a grid with wires of diameter $2r$ separated by a distance ξ, the shielding inefficiency in the limit of small $2\pi r / \xi$ can be written as:

$$\sigma = (\xi / 2\pi c) \log(\xi / 2\pi r). \qquad (2.7)$$

A value for σ of less than 1% can easily be obtained even though a problem is introduced by the grid itself since a certain fraction of the charge, λ, will be collected on the grid instead of on the anode. In the event of this fraction of charge being constant, the charge collection problem on the grid becomes negligibly small, but then the fraction depends somewhat on the orientation of the ionising track relative to the electrodes. Furthermore, it is desirable to keep λ as small as possible.

Figure 2.2 shows $(1-\lambda)$ as a function of the ratio of the field between the grid and collecting electrode to that in the body of the detector [WI50b] for some values of $2\pi r / \xi$.

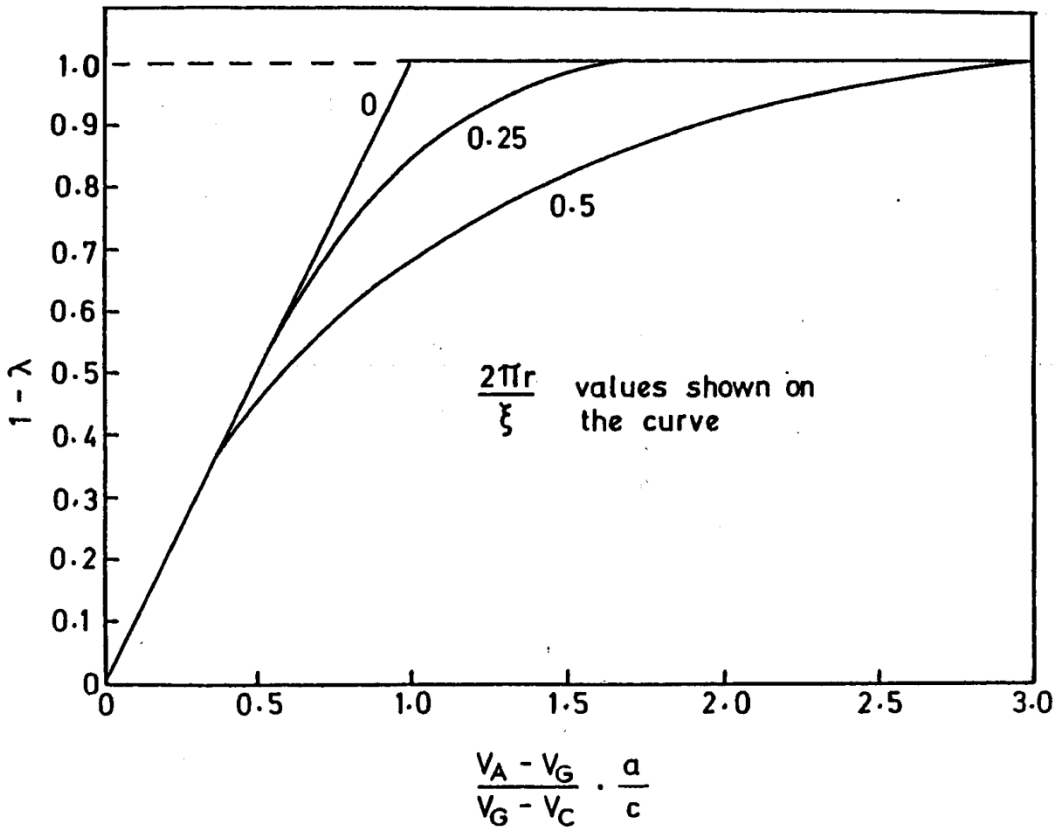

Figure 2.2: The dependence of charge losses to the grid on the ratio of the field strengths [WI50b].

Complete electron collection at the anode is established when

$$\frac{V_A - V_G}{V_G - V_C}\frac{a}{c} \geq \frac{1+(2\pi r/\xi)}{1-(2\pi r/\xi)}. \tag{2.8}$$

The above condition, which places a limitation on the choice of the operating voltages, may be easily satisfied, but even then a small fraction of the electrons may be lost to the grid due to two processes, in particular, the diffusion of electrons and recombination of electron and positive-ion pairs. The recombination of the ion-electron pairs (e.g. X^+ and e^-) in the case of no electric field, usually occurs under the force of their electric attraction, thereby emitting a photon in the process [LE87]

$$X^+ + e^- \rightarrow X + h\nu. \tag{2.9}$$

For molecular ions (e.g. X^- and Y^+), a similar recombination reaction occurs [LA07]

$$X^- + Y^+ \rightarrow XY^* \rightarrow XY^+ + e^-. \quad (2.10)$$

These effects tend to get worse for low field strengths and high gas pressures. Furthermore, additional signal losses usually occur if some electronegative impurities, such as oxygen, are present in the gas. Consequently, the ionisation electrons may become attached to the impurities and form slow moving negative ions [LE87]:

$$e^- + X \rightarrow X^- + h\nu. \quad (2.11)$$

Therefore, maintaining the purity and continuous steady flow of the gas used is essential. In conclusion, a linear response from the ionisation detector can be achieved by the collection of signals which are entirely due to the primary ions.

The production of secondary ionisation by electron impact, a phenomenon called gas amplification, usually occurs if the ratio of field strength to gas pressure becomes high enough. This phenomenon places a further limitation on the choice of the field strengths inside the detector.

2.2 Heavy-ion elastic scattering

The elastic scattering of complex nuclei on nuclei has been studied mainly for two reasons. Firstly, for the determination of potentials in terms of the simplest optical model which are then subsequently employed in the analysis of direct reactions (transfer and inelastic scattering) and secondly, for the testing of different more refined models of nucleus-nucleus potential, which depend on the nuclear structure properties of the nuclei involved [OE75]. Charged particle scattering at incident energies below the Coulomb barrier is referred to as Coulomb scattering. It occurs in two different forms [BE64] namely, Rutherford scattering where non identical nuclei collide and Mott scattering that is due to the collision of identical particles. Section 2.2.1 describes the details of Rutherford scattering that takes place and in order to interpret the Rutherford scattering data, the following Section 2.2.3, presents a description of the optical model of elastic scattering [FE54], a model that is used to analyse the scattering data since it involves nuclear interaction between the colliding nuclei.

2.2.1 Rutherford scattering

The present work involves the application of the Rutherford scattering. This type of elastic scattering is the result of a collision of a moving charged particle with an atomic nucleus. The scattered particle is assumed to traverse in a hyperbolic path in the case of unbound orbits in a $1/r^2$ force as shown in Fig. 2.3. The projectile is considered to approach the target nucleus along a straight line that passes a distance b (impact parameter) from the nucleus in the absence of a repulsive force, and is scattered through an angle θ. In the case of the projectile being very far from the target, the projectile attains negligible Coulomb potential energy, whereas on the other hand, if the projectile passes close to the target, the projectile reaches a minimum separation distance $r_{\min}$, which depends on b, with a head-on collision taking place when $b = 0$ and the projectile reversing its trajectory motion [KR88].

In the non-relativistic case, at a distance d of closest approach, the initial kinetic energy (KE) is converted to Coulomb potential energy [KR88] given by

$$\frac{1}{2}mv_0^2 = \frac{1}{4\pi\varepsilon_0}\frac{Z_1 Z_2 e^2}{d}, \tag{2.12}$$

where $Z_1 e$ is the charge of the projectile and $Z_2 e$ is the charge of the target.

The differential cross-section for a Rutherford scattering reaction of spinless particles in the centre-of-mass (c.m.) reference frame is given by

$$\frac{d\sigma}{d\Omega_{\text{c.m.}}} = \frac{Z_1 Z_2 e^2}{4\pi\varepsilon_0}\left(\frac{1}{4E_{\text{c.m.}}}\right)^2 \left(\frac{1}{\sin^4\frac{\theta_{\text{c.m.}}}{2}}\right), \tag{2.13}$$

where $E_{\text{c.m.}}$ is the centre-of-mass energy of the projectile and $\theta_{\text{c.m.}}$ is the centre-of-mass scattering angle.

Equation (2.13) shows that the Rutherford scattering cross-section is strongly dependent on the scattering angle. Furthermore, the formula breaks down when $E_{\text{c.m.}}$ increases to a point where projectile and target surfaces touch.

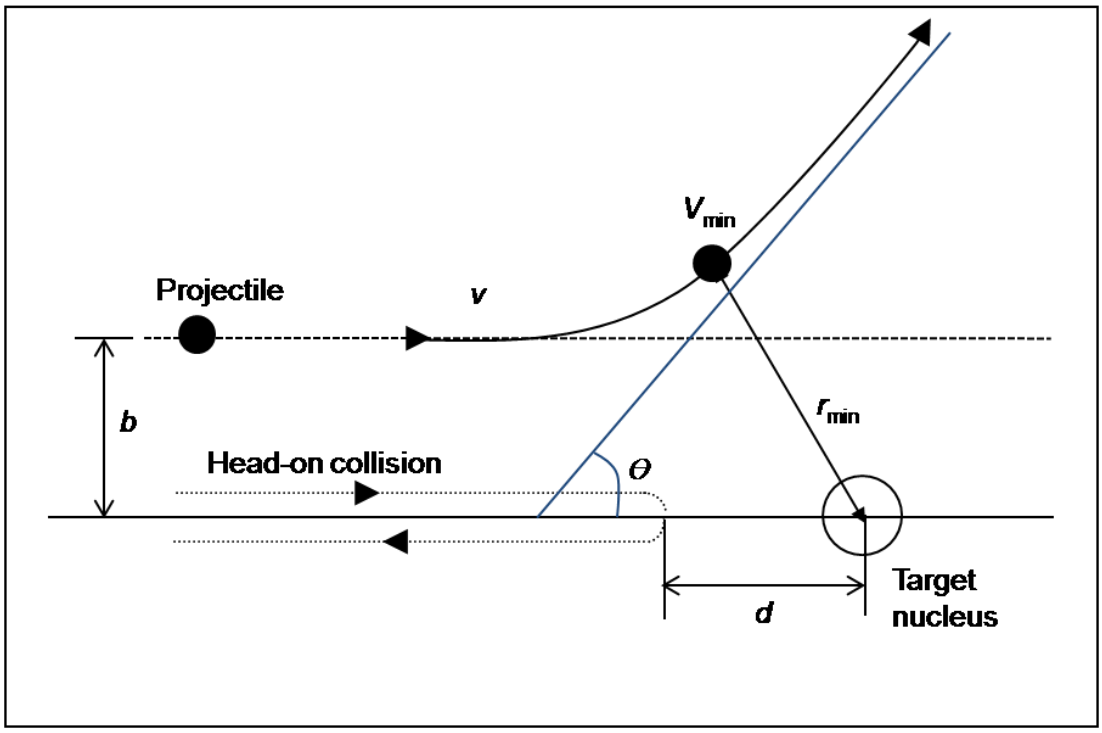

Figure 2.3: Path followed by a charged particle undergoing Rutherford scattering.

2.2.2 The Schrödinger equation for scattering

In order to calculate the cross-section we need the scattering amplitude and as a result to calculate the scattering amplitude, the scattered wave function is needed. In principal this can be generated from the Schrödinger equation for $A_a + A_A$ interacting nucleons (where subscripts, *a*, *A* are *projectile* and *target* respectively), provided the nucleon-nucleon potential [GL83] is known. Out of the solutions of such a scheme would drop the cross-sections for all possible reaction channels, etc. Of course, this is utterly unrealistic. The nuclear force is certainly not fully understood; even if it were, the computational complexity of such a scheme is beyond consideration.

A much more modest scheme is utilised in order to progress, hence: one needs to postulate a potential that describes the interaction between the incident and target nucleus and describe the reaction as a two-body interaction [ME58]. However, the formulation must include the excitation and reaction of the nuclei involved. Given such a potential $V(r)$, the wave function can be calculated from the Schrödinger equation:

$$\left[-\frac{\hbar^2}{2m}\nabla^2 + V(\mathrm{r})\right]\psi(\mathrm{r}) = E\psi(\mathrm{r}) \tag{2.14a}$$

or

$$H\psi(\mathrm{r}) = E\psi(\mathrm{r}). \tag{2.14b}$$

For scattering problems it is useful to write the above equation in the form

$$\left[\nabla^2 - U(\mathrm{r}) + k^2\right]\psi(\mathrm{r}) = 0, \tag{2.15}$$

where $k = \left[2mE/\hbar^2\right]^{1/2}$ and $U = 2mV/\hbar^2$.

The Hamiltonian for the scattering problem can be expressed as:

$$H = H_a + H_A - \frac{\hbar^2}{2\mu_\alpha}\nabla_\alpha^2 + V_\alpha, \tag{2.16}$$

where μ_α is the reduced mass of the system. The energy E is the total energy of the system (it includes excitation of internal states). The wave function of the system can be expanded using the complete sets ψ_a and ψ_A:

$$\psi = \sum_{a'A'} \chi_{a'A'}(\mathrm{r}_\alpha)\psi_{a'}\psi_{A'}. \tag{2.17}$$

The Schrödinger equation with the Hamiltonian expression is given by

$$\left[H_a + H_A - \frac{\hbar^2}{2\mu_\alpha}\nabla_\alpha^2 + V_\alpha\right]\psi = E\psi. \tag{2.18}$$

If $H_a\psi_a = \varepsilon_a\psi_a$, for example, Eq. (2.18) becomes

$$\sum_{a'A'}\left[(\varepsilon_{a'} + \varepsilon_{A'} - E) - \frac{\hbar^2}{2\mu_\alpha}\nabla_\alpha^2 + V_\alpha\right]\chi_{a'A'}(\mathrm{r}_\alpha)\psi_{a'}\psi_{A'} = 0. \tag{2.19}$$

Multiply from the left by $\psi_a^*\psi_\mathrm{A}^*$ and integrate over the integral coordinates to get

$$\left[\nabla_\alpha^2 - U_{aAaA}(\mathrm{r}_\alpha) + k_{aA}^2\right]\chi_{aA}(\mathrm{r}_\alpha) = \sum_{\substack{a' \neq a \\ A' \neq A}} \chi_{a'A'}(\mathrm{r}_\alpha)U_{aAa'A'}(\mathrm{r}_\alpha), \tag{2.20}$$

where $k_\alpha^2 = 2\mu_\alpha(E-\varepsilon_a-\varepsilon_A)/\hbar^2$ and

$$U_{\alpha A a' A'} = \frac{2\mu_\alpha}{\hbar^2}\iint \psi_a^* \psi_A^* V_\alpha \psi_{a'} \psi_{A'} dr_a r_A = \frac{2\mu_\alpha}{\hbar^2}\left\langle aA\middle|V_\alpha\middle|a'A'\right\rangle. \tag{2.21}$$

This equation describes the scattering for a particular incident channel by a potential appropriate to that channel, with the coupling to all other possible excitations and configurations on the right hand side. There is an equation of this sort for each possible incident channel, *aA*. This is an infinite set of coupled equations and there are no ways of solving it exactly. To progress approximations are made and models are used to determine the important features that are required to be described. We may assume that only a few channels are important and thus retain only a few in the infinite set: this leads to the *coupled channels approximation*. Alternatively, one may model the effect of many reaction channels by an *absorptive* term in the potential: this leads to the *optical model*.

2.2.3 The optical model of heavy-ion elastic scattering

The optical model also known as the "*Cloudy Crystal Ball Model*" [KR88], is a model that describes elastic scattering of charged particles in the presence of absorptive effects. In the Schrödinger equation appropriate to elastic nuclear scattering, a simple two-body interaction potential, $U(r)$, represents the many-body interaction between colliding nuclei. The potential $U(r)$ is spherically symmetric and depends on the separation distance, r, between the centre-of-mass of the projectile and the centre-of-mass of the target. Thus, for the scattering of charged spinless nuclei, it can be written as:

$$U(r) = U_{\mathrm{C}}(r) + U_{\mathrm{N}}(r), \tag{2.22}$$

where $U_{\mathrm{N}}(r)$ is the short-range attractive nuclear interaction and $U_{\mathrm{C}}(r)$ is the long-range repulsive Coulomb interaction.

The nuclear interaction $U_{\mathrm{N}}(r)$ is taken to be a complex potential defined by

$$U_{\mathrm{N}}(r) = V(r) + iW(r), \tag{2.23}$$

where $V(r)$ represents the real part responsible for elastic scattering and $iW(r)$ is the imaginary part responsible for absorption of incoming flux into inelastic scattering channels.

In analogy to the refraction and absorption of light by a semi-transparent sphere, Eq. (2.23) is called the optical potential and its incorporation into the Schrödinger equation results in the optical model.

The interaction potential given by Eq. (2.22) is inserted into the Schrödinger equation which, in the centre-of-mass system, describes the scattering of a projectile of energy E and reduced mass μ. An expansion of the total scattering waveform in terms of Legendre polynomials is performed and after some algebraic manipulation the radial wave equation is obtained [JA70c]:

$$\left[\frac{d^2}{dr^2}+\frac{2\mu}{\hbar^2}(E-U(r))-\frac{\ell(\ell+1)}{r^2}\right]f_\ell(kr)=0. \qquad (2.24)$$

Equation (2.24) is the result of the expansion of wave functions in terms of Legendre polynomials, where $f_\ell(kr)$ is the radial wave function for a particular value ℓ of angular momentum of relative orbital motion. Therefore, explicit forms for $U_N(r)$ and $U_C(r)$ are required in order to solve the above equation.

Ideally, $U_C(r)$ should represent the Coulomb interaction between the charge distributions of the projectile and target, including their diffuse surface nature. However, Woods and Saxon [WO54] and Glassgold and Kellogg [GL57] showed that scattering at low energies is insensitive to the details of the nuclear charge distribution. Thus, the Coulomb potential for charged particle scattering is expressed as [JA70d]:

$$U_C(r)=\frac{Z_1Z_2e^2}{r}, \qquad r > R_C \qquad (2.25a)$$

$$U_C(r)=\frac{Z_1Z_2e^2}{2R_C}\left[3-\left(\frac{r^2}{R_C^2}\right)\right], \qquad r \le R_C \qquad (2.25b)$$

$$R_{\mathrm{C}} = \left[\frac{5}{3}\left\langle r^2 \right\rangle\right]^{1/2}, \tag{2.26}$$

where $< r^2 >$ is the mean-square charge radius determined from electron scattering.

The Woods-Saxon [WO54] form is physically plausible and numerically very suitable in investigations involving heavy-ion scattering and is given by

$$U_{\mathrm{N}}(r) = \left[V_0 f_{\mathrm{R}}(r) + iW_0 f_{\mathrm{I}}(r)\right], \tag{2.27}$$

$$f_{\mathrm{R,I}}(r) = \left[1 + \exp\left(\frac{r - R_{\mathrm{R,I}}}{a_{\mathrm{R,I}}}\right)\right]^{-1}, \tag{2.28}$$

where $a_{\mathrm{R,I}}$ are surface diffusenesses and $R_{\mathrm{R,I}}$ are the nuclear potential radii for the real and imaginary parts.

From Eq. (2.28), the nuclear potential radii $R_{\mathrm{R,I}}$ are expressed in the form $R_{\mathrm{R,I}} = R_{0\mathrm{R,I}}(A_1^{1/3} + A_2^{1/3})$ for the heavy-ions whereas $R_{\mathrm{R,I}} = R_{0\mathrm{R,I}}(A_2^{1/3})$ for the light-ion convention with A_1 being the mass of the projectile and A_2 being that of the target. The imaginary part of the nuclear potential described by Eqs. (2.27) and (2.28) represents volume absorption.

By taking the first derivative of Eq. (2.28), we get

$$W(r) = -W_1 \frac{4\exp\left(\dfrac{r - R_{\mathrm{I}}}{a_{\mathrm{I}}}\right)}{\left[1 + \exp\left(\dfrac{r - R_{\mathrm{I}}}{a_{\mathrm{I}}}\right)\right]^2}. \tag{2.29}$$

Equation (2.29) gives an imaginary potential that is surface peaked (since valence nucleons at the surface can easily participate in nuclear reactions) [AU78]. However, the volume Woods-Saxon potential was used in the analysis for absorption.

The radial wave equation may be solved only numerically with the forms of the interaction potential given by Eqs. (2.25a, b) and (2.27). At large separation distances

r the nuclear field is negligible and numerical solutions of $f_\ell(kr)$ are matched to known Coulomb wave-functions to determine nuclear phase shifts δ_ℓ. The phase shift δ_ℓ is a complex quantity since the interaction potential $U(r)$ is complex. All the information of the scattering process is contained in δ_ℓ [JA70].

The scattering amplitude $f(\theta)$ may be expressed in terms of δ_ℓ [JA70] as:

$$f(\theta) = \frac{1}{2ik}\sum_{\ell=0}^{\infty}(2\ell+1)(S_\ell - 1)P_\ell(\cos\theta), \tag{2.30}$$

where the elastic scattering S-matrix, S_ℓ, is given by

$$S_\ell = \exp(2i(\sigma_\ell + \delta_\ell)), \tag{2.31}$$

and σ_ℓ are the analytically known Coulomb phase shifts due to scattering from the pure Coulomb potential due to a point charge. It follows then that

$$e^{2i(\sigma_\ell+\delta_\ell)} + 1 = (e^{2i\sigma_\ell} - 1) + e^{2i\sigma_\ell}(e^{2i\delta_\ell} - 1), \tag{2.32a}$$

where the complex scattering amplitude is identified as $e^{2i\delta_\ell}$ and hence the reflection coefficient is given by

$$|\eta_\ell| = \left|e^{2i\delta_\ell}\right|. \tag{2.32b}$$

Therefore, the scattering amplitude can be regarded as a summation of Coulomb and nuclear amplitudes [JA70], hence:

$$f(\theta) = f_{\mathrm{C}}(\theta) + f_{\mathrm{N}}(\theta), \tag{2.33}$$

and the elastic scattering cross-section is given by

$$\frac{d\sigma}{d\Omega} = |f(\theta)|^2. \tag{2.34}$$

A fit to elastic scattering data is obtained by varying one or more of the six optical parameters, (V_0, $R_{0\mathrm{R}}$, a_{R}, W_0, $R_{0\mathrm{I}}$, a_{I}). These fits are not unique and are subject to ambiguities, the best known of which is the Igo ambiguity [JA70].

Chapter 3

The C-line and Δ*E*-*E* gas-ionisation detector

This chapter presents a description of the newly refurbished C-line and its alignment, the Δ*E*-*E* gas-ionisation detector gas delivery system, the procedures that were followed during the use of the Δ*E*-*E* gas-ionisation detector gas delivery system and the characteristics of the Δ*E*-*E* gas-ionisation detector. The heavy-ion scattering measurement using the Δ*E*-*E* gas-ionisation detector, details of the associated electronics and the data acquisition system are presented.

3.1 The newly refurbished C-line

The newly refurbished C-line shown in Fig. 3.1 consists of the following:

(a) Quadrupole magnet: This magnet is responsible for *particle beam focussing*, since the magnet creates a magnetic field whose magnitude grows rapidly with radial distance from its longitudinal axis.

(b) Faraday cups: These are metallic cups with an off-set quartz disc base (monitored by a camera) designed to stop the charged particle beam. The beam current measured is used to determine the transmission and focussing requirements of the beam down the line.

(c) Adjustable line slits: These are responsible for controlling the physical width of the beam and its angular spread.

(d) Large scattering chamber: This is an 86 cm (30″) diameter aluminium chamber mounted along the beam line. The chamber is used for measuring the angular distributions of the charged particles emitted in different nuclear reactions.

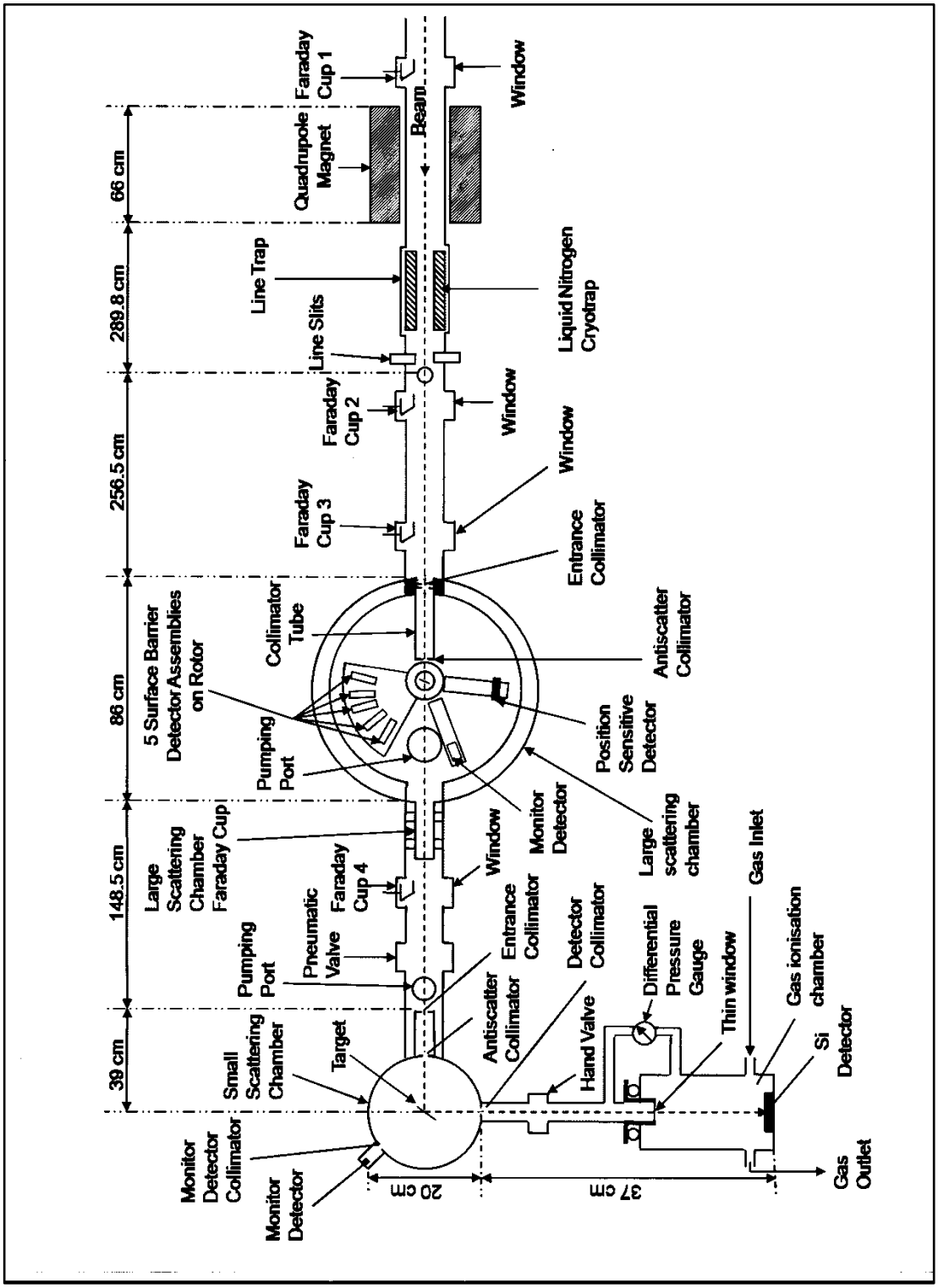

Figure 3.1: The schematic diagram of the C-line and associated equipment at the EN Tandem accelerator of iThemba LABS (Gauteng).

(e) Small scattering chamber: Provides the same function similar to that offered by the large scattering chamber but only that it has a smaller diameter (20 cm) and has the detector directly coupled to the off-set moveable lid.

(f) Δ*E*-*E* gas-ionisation detector: Detects the scattered particles that are produced during a scattering reaction and allows the identification of the reaction products and the determination of the corresponding kinetic energy.

(g) Entrance and anti-scatter collimators: These collimators are responsible for the production of a quasi-parallel beam. These are crucial elements in determining the sensitivity and resolution of the charged particle detectors. The collimators give a beam angle-divergence at the target of < 0.2º required for acceptable kinematic spread.

(h) Liquid nitrogen cryotrap: Placed between the large scattering chamber and the diffusion pump, prevents contamination of the targets by carbon and silicon arising from the back-streaming of diffusion-pump oil.

3.2 Alignment of the C-line

The entrance collimator, target centre and the detector collimator(s) of the scattering chambers were aligned on the same optical line of sight through the use of a *theodolite*. This is an optical instrument that consists of a small mounted telescope rotatable in horizontal and vertical planes with reference points provided by the analyser and switching magnets of the accelerator. In addition, during the alignment procedure, all the beam line components, Faraday cup cross-wires, line slits, quadrupole magnet, together with the components already mentioned for both the large and the small scattering chambers were moved until they were all on the same line of sight.

The Δ*E*-*E* gas-ionisation detector has an angular movement between -20º < θ_{Lab} < 135º made possible by rotating the upper part of the small scattering chamber around the target position. A monitor detector can be mounted at an angle of 45º below the target, which allows normalisation between runs during data collection. A circular entrance collimator of 1.2 mm diameter allowed the beam to enter the small scattering chamber, being followed by an anti-scatter collimator of 2.5 mm diameter. A detector collimator of 1 mm diameter was used for the Δ*E*-*E* gas-ionisation

detector which was mounted in a port of the moveable upper part of the small scattering chamber. Final alignment of the Δ*E*-*E* gas-ionisation detector to within ± 0.2^{o} was achieved by minimising the difference between left/right elastic scattering of a 29.0 MeV ^{16}O beam from a thin ^{58}Ni foil.

3.3 Δ*E*-*E* gas-ionisation detector gas delivery system

The schematic diagram of the Δ*E*-*E* gas-ionisation gas delivery system is shown in Fig. 3.2. The main function of the Δ*E*-*E* gas-ionisation gas delivery system was to transport the iso-butane gas to the Δ*E* part of the Δ*E*-*E* gas-ionisation detector.

Figure 3.3 shows a photograph of the Δ*E*-*E* gas-ionisation detector gas delivery system mounted on a moveable trolley and beam line components.The present Δ*E*-*E* gas-ionisation gas delivery system consisted of four main components which were crucial for the elastic-scattering reaction of ^{16}O on ^{28}Si to take place. These were:

- the *Iso-butane gas cylinder*,
- the *Iso-butane gas delivery system*,
- the *Small scattering chamber* and
- the Δ*E*-*E gas-ionisation chamber*.

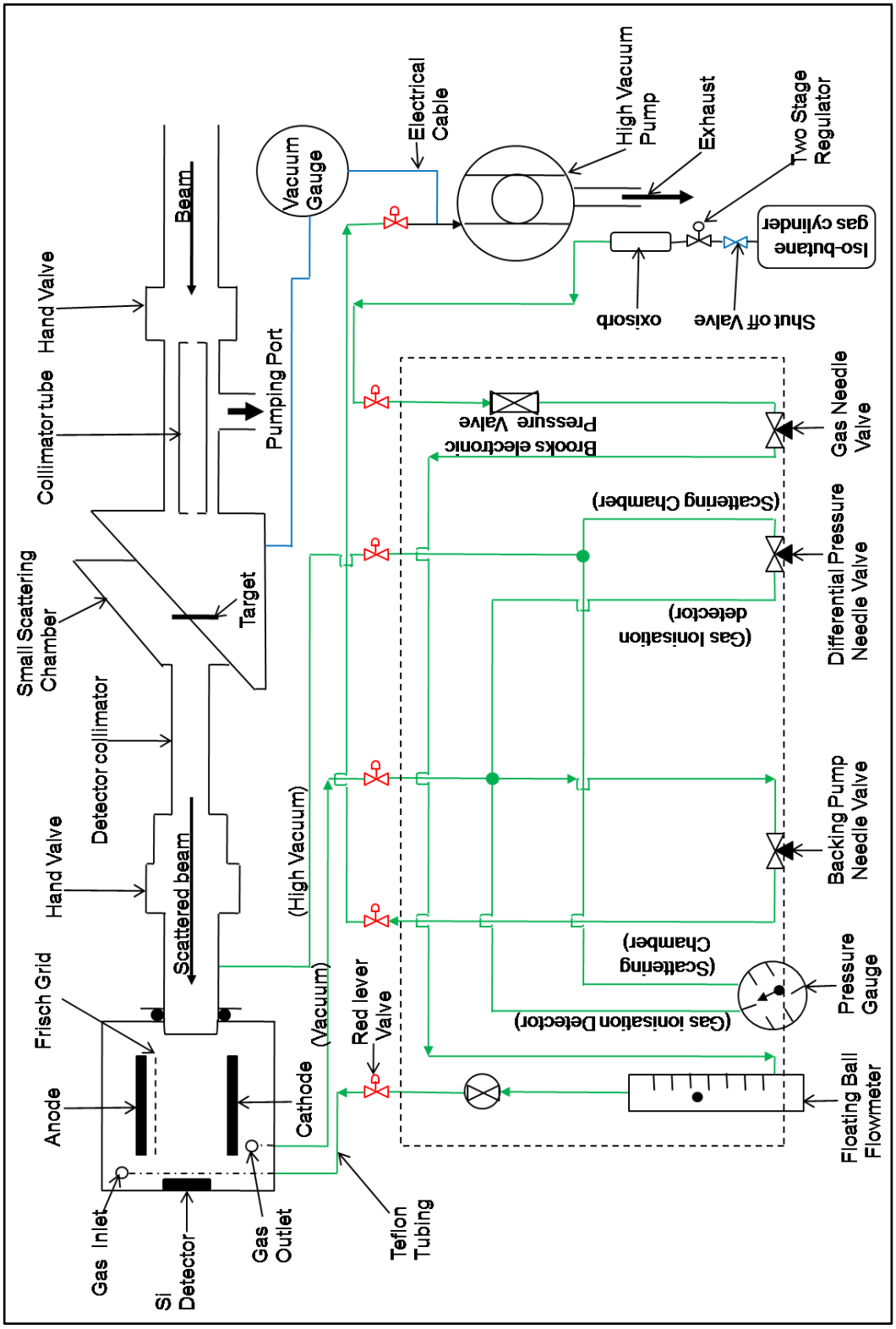

Figure 3.2: A schematic diagram of the Δ*E*-*E* gas-ionisation detector gas delivery system.

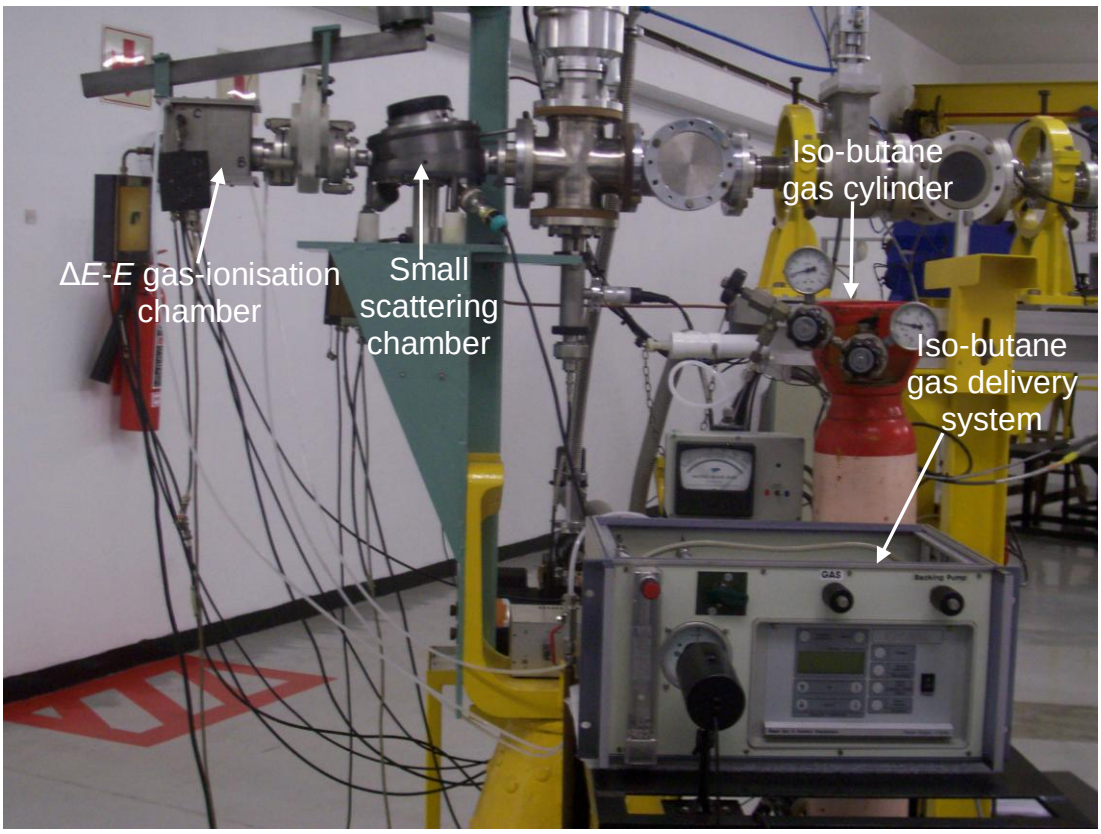

Figure 3.3: Photograph of the Δ*E*-*E* gas-ionisation detector gas delivery system mounted on a moveable trolley and beam line components.

3.3.1 Iso-butane gas delivery system

This part of the system was responsible for transporting and controlling the iso-butane gas used in the Δ*E* part of the Δ*E*-*E* gas-ionisation detector which flowed through teflon tubing (impervious to the diffusion of oxygen from the air). It consisted of three main valves, namely the (i) Backing pump valve (ii) Black gas valve and (iii) Floating ball flow-meter valve which are indicated in Fig. 3.4. The presence of the Brooks electronic pressure control system in this part enabled the differential pressure between the two sides of the thin mylar window separating the Δ*E* part of the detector from the high vacuum of the small scattering chamber to be kept constant within acceptable limits (± 5% of set pressure of 1 kPa). The differential pressure was monitored by a mechanical, high precision, gauge (see Fig. 3.4) using the image from a CCD camera displayed in the accelerator control room.

3.3.2 Iso-butane gas cylinder

The iso-butane gas cylinder was the source of iso-butane gas (chemical purity: 99.95%) that was used for the ionisation process of the ions entering the Δ*E* part of the Δ*E*-*E* gas-ionisation detector. The iso-butane gas cylinder and regulator consisted of four main valves that were responsible for controlling the flow direction of the ionising iso-butane gas, namely the

(i) Regulator pressure valve,

(ii) Regulator outlet valve,

(iii) Gas outlet valve and

(iv) Main central cylinder gas valve (see Fig 3.4).

Tables 3.1, 3.3, and 3.2 describe in detail the steps that were carried out during the safety check, starting up and shutting down procedure of the Δ*E*-*E* gas-ionisation detector gas delivery system.

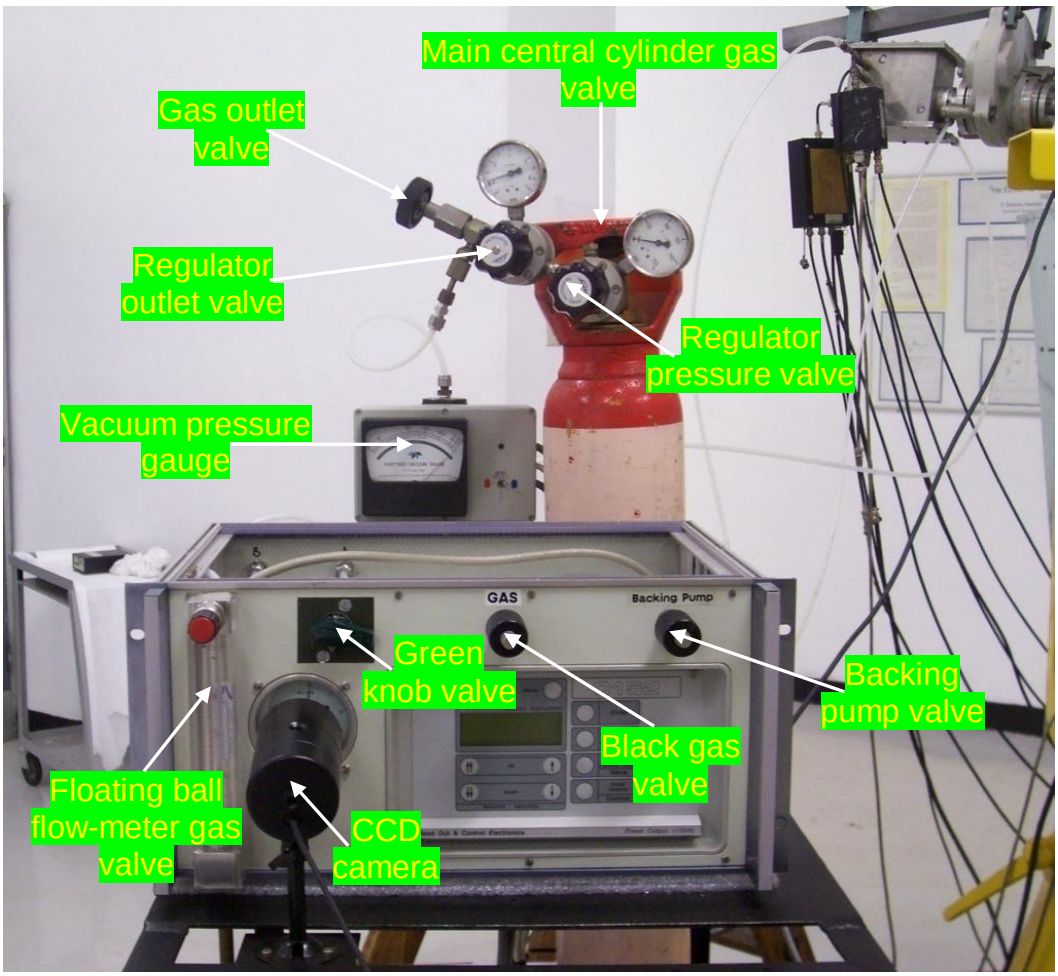

Figure 3.4: Photograph of the Δ*E*-*E* gas-ionisation detector gas delivery system set-up and the associated valves.

Table 3.1: Safety checks before starting up the Δ*E*-*E* gas-ionisation detector gas delivery system.

Step	Procedure
1	The Main central cylinder gas valve must be tightly closed.
2	The two Regulator valves (Pressure and Outlet) coupled to the Gas cylinder tank must be closed.
3	The Gas outlet valve also coupled to the Gas cylinder tank must be closed.
4	The Floating ball flow-meter gas valve coupled to the iso-butane gas delivery system must be closed.
5	The Black gas valve at the front of the iso-butane gas delivery system must be closed.
6	The Backing pump valve that is coupled to the iso-butane gas delivery system must be fully opened.

Table 3.2: Δ*E*-*E* gas-ionisation detector gas delivery system shutting down procedure.

Step	Procedure
1	Set the "*set-point percentage*" value on the iso-butane gas delivery system to zero.
2	Close the Black gas valve in a clockwise direction.
3	Turn the Green knob valve into a horizontal position.
4	Close the Main central cylinder gas valve in a clockwise direction.
5	Close the Gas outlet valve in an anti-clockwise direction.
6	Close the Regulator pressure valve in an anti-clockwise direction.
7	Close the Outlet regulator valve in an anti-clockwise direction.
8	Close the Floating ball flow-meter gas valve in a clockwise direction.

Table 3.3: Δ*E-E* gas-ionisation detector gas delivery system starting up procedure.

Step	Procedure
1	Switch on the iso-butane gas delivery system.
2	Open the Main central cylinder gas valve in an anti-clockwise direction.
3	Open the Regulator pressure valve in a clockwise direction.
4	Open the Regulator outlet valve in a clockwise direction.
5	Open the Gas outlet valve in an anti-clockwise direction.
6	Open the Black gas valve in an anti-clockwise direction.
7	Open the Floating ball flow-meter gas valve in an anti-clockwise direction.
8	Ensure that the Green knob valve at the front of the iso-butane gas delivery system is in a vertical position when in use (the knob isolates the gas-ionisation detector from the High vacuum section).
9	Always ensure that the Red lever valve (above copper pump line) directly coupled to the Teflon tubing coming from the "*Backing pump In*" section of the iso-butane gas delivery system is opened. The lever must be facing in a downward direction.
10	Select the "*set-point option* (*given in % form*)" displayed on the screen of the iso-butane gas delivery system and press the "*enter*" key to confirm the selected option.
11	Press the "*control mode* /*valve control*" key on the iso-butane gas delivery system until a 'V-' output is displayed and press the "*enter*" key to confirm the chosen valve function setting.
12	Press the "*control mode* /*valve control*" key again until a 'V0' output is displayed on the screen and press the "*enter*" key to confirm the new valve function setting.
13	Change the gas flow-rate setting on the iso-butane gas delivery system by increasing the percentage flow-rate in steps of 20 using the "*double arrow up/down*" keys until a steady flow-rate is achieved.

Note: A steady and useable differential pressure of 1 kPa was achieved at a flow-rate of 60% on the iso-butane gas delivery system and at a Vacuum pressure gauge reading at the backing pump of the system of approximately 23 - 30 μm of Hg.

3.4 Optimisation and testing of the EN Tandem accelerator

During the test, an extraction voltage of 25 keV was used to determine the energy of the extracted negative ions from the 860 C sputter ion source employing a graphite target. A series of negative ions, C^-, C_2^-, C_3^-, $^{16}O^-$ etc. were then identified as shown in Fig. 3.5. The results of the test were latter presented [JI08] at a SAIP Conference that was held at the University of Limpopo. Furthermore, the same ion source was also used to produce a ^{12}C beam that was used during the preliminary alignment checks of the C-line.

The procedure for an inflection magnet scan with an extraction voltage of 25 keV for the 860 C ion source was carried out as follows:

Stage One: Readings of the low energy cup current and inflection magnet current were taken. The values of the low energy cup and inflection magnet currents are given in the appendix.

Stage Two: A relationship between the inflection magnet current and the mass of the negative ions was derived. The equation was given by

$$I_{in} = \mathrm{S}\frac{F\sqrt{m}}{q\sqrt{2qV}}, \tag{3.1a}$$

where S is a constant, F is the magnetic force on the ion, q is the charge of the ion, V is the velocity of the ion, and m is the mass of the negative ion.

Equation (3.1a) was simplified to the following expression:

$$I_{in} = k\sqrt{m} \tag{3.1b}$$

where

$$k = \mathrm{S}\left[\frac{F}{q\sqrt{2qV}}\right].$$

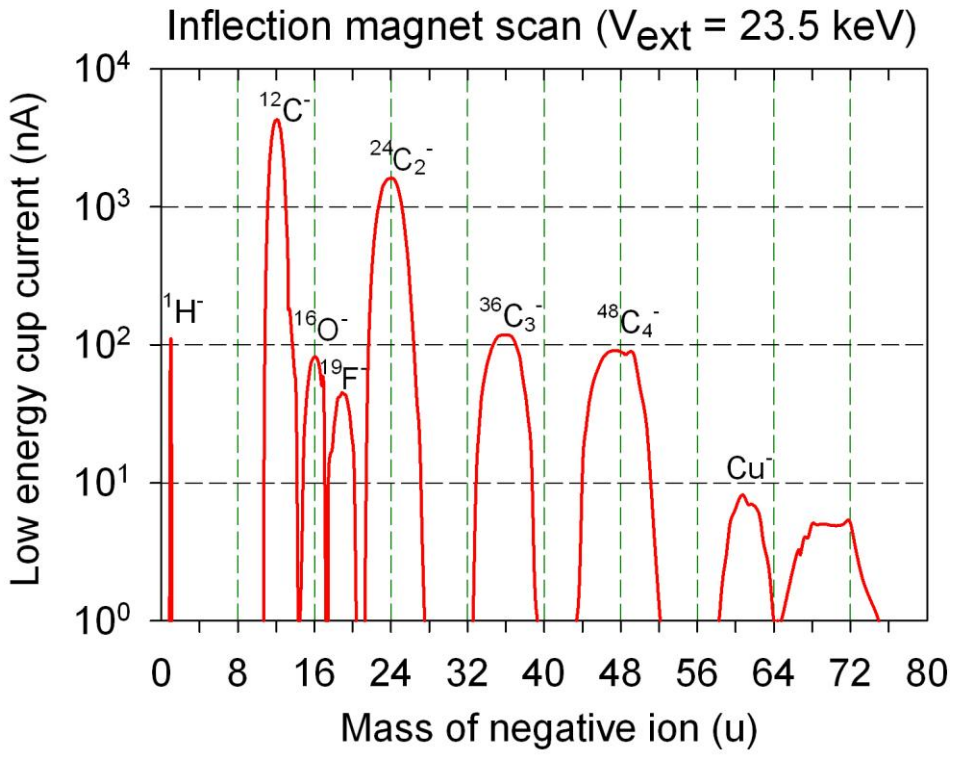

Figure 3.5: The extracted negative ions after an inflection magnet scan of an 860 C sputter ion source employing a graphite target.

Equation (3.1b) was further utilised in the derivation of a calibration curve that was given by

$$M = \left[\frac{I_{in} + 0.615}{4.102} \right]^2, \tag{3.2}$$

where M is the mass of the negative ion and I_{in} is the inflection magnet current.

3.5 Characteristics of the Δ*E*-*E* gas-ionisation detector

A diagrammatic layout of the Δ*E*-*E* gas-ionisation detector is shown in Fig. 3.6. The body of the detector, the anode and the cathode are made of stainless steel, with the electrodes being highly polished. The frame of the Frisch grid is made of brass, while the grid itself is constructed from Cu-Be wires of 0.05 mm in diameter, with 0.5 mm spacing intervals, which are oriented perpendicularly to the trajectory of the particles. Insulators made of macor are used as mounts for the anode, grid and cathode.

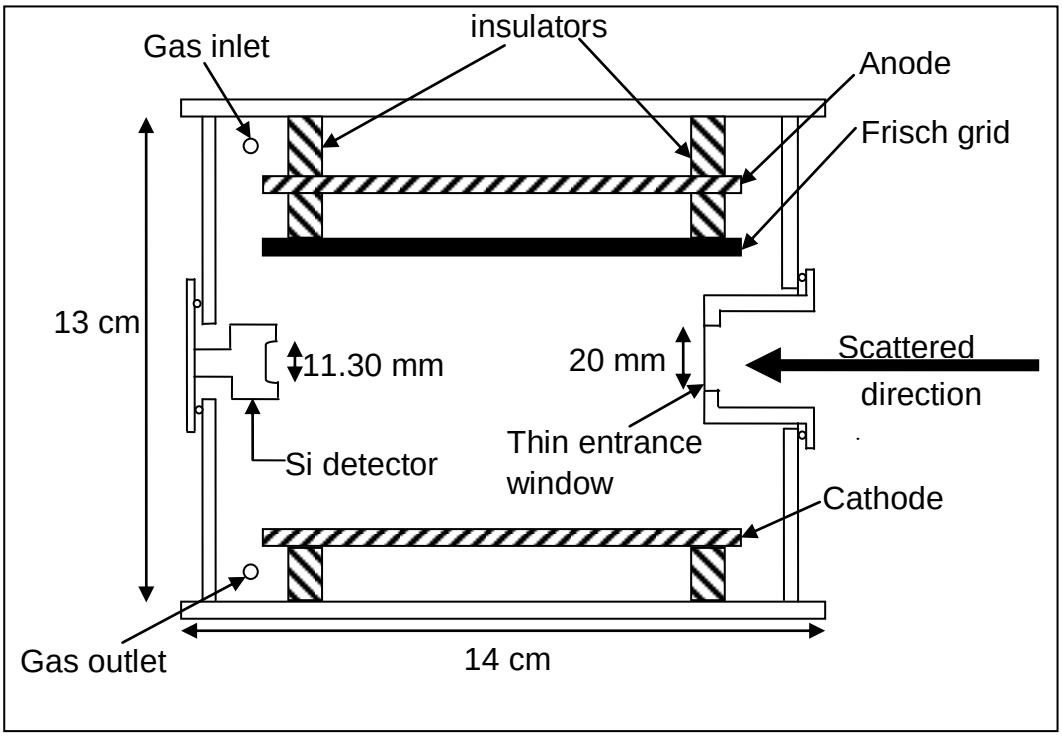

Figure 3.6: Schematic diagram of the Δ*E*-*E* gas-ionisation detector.

The spacing between anode and grid is 20 mm, and 64 mm between the grid and cathode. Both the entrance window and the solid-state detector extend into the detector in a way such that the length (12.4 cm) of the Frisch grid covers the length (10 cm) of the particle trajectory inside the chamber [CA81]. The solid-state silicon surface-barrier detector has an active area of approximately 100 mm^2 (diameter 11.30 mm) and a specified energy resolution of 17 keV for α-particles

(**Ortec:** BF-17-100-100). The resolution of the detector was found to be 24 keV (FWHM) for the 5.486 MeV line of a thin ^{241}Am alpha source.

The entrance window is made from mylar of 2.0 µm thickness glued over a vertical rectangular slot 20 mm high and 10 mm wide in a stainless steel holder. Previously, 1 µm and 0.25 µm parylene entrance windows supported by a Ni wire mesh of 97% transparency were used. The Ni wires of diameter 0.0135 mm were spaced at intervals of 1.25 mm over the entire surface area of the window. As a precaution against unexpectedly high differential pressure during the testing of the newly refurbished gas pressure control system, the 2 µm thickness mylar entrance window was used which could withstand pressures exceeding 10 times the normal operating pressure of 1 kPa.

Particles enter the ΔE-E gas-ionisation detector through the thin window which serves to contain the continuously flowing detector iso-butane, and in addition supports a differential pressure of 1 kPa over a long time period. The continuous flow of the iso-butane gas was used to minimise the contamination of the gas by electronegative impurities which cause signal losses due to electron attachment. Contamination was further minimised by passing the iso-butane gas through an OXISORB filter (absorbs oxygen and moisture from the gas). The differential iso-butane gas pressure across the thin window could be maintained stable to within 0.02 kPa, at a pressure of 1 kPa, over a period of 24 hours.

The shielding inefficiency parameter, σ, of the grid given by Eq. (2.7) was calculated to be 0.2% from the wire diameter and spacing given previously. However, it should be bourne in mind that from Eq. (2.8) the minimum ratio of grid-anode to grid-cathode field strengths necessary for prevention of electron loss the grid has to be greater than or equal to 1.92 (right hand side value Eq. (2.8) the geometrical constraint). In order to determine the most suitable operating voltages for the electrodes, the response of the ΔE detector as a function of the field strengths inside the chamber was measured using a 23 MeV $^{16}O^{5+}$ beam scattered from a ^{58}Ni target. The energy-loss signal ΔE of ^{16}O beam scattered from ^{58}Ni was collected with the ΔE-E gas-ionisation detector positioned at a forward scattering angle of 20° with the differential pressure set to 1 kPa. Whilst maintaining the potential difference

between the anode and the grid at a constant value of 150 V (used in previous measurements), the ΔE peak maximum obtained in a 1024 channel spectrum as a function of grid-cathode potential difference was measured. The results are shown in Fig. 3.7. Here, it can be seen that best ΔE detector performance can be achieved for a value ($V_G - V_C$) = 60 V. The ΔE peak maximum as a function of the anode-grid potential difference was then measured while maintaining the potential difference between grid and cathode at a constant value of 60 V. These results are shown in Fig. 3.8. Tabulated values of the results for the two operations are given in the Appendix.

Figure 3.8 shows that, as the potential difference between anode and grid is increased from zero, the fraction of charge collected by the grid decreases and as a result the channel position increases until, when Eq. (2.8) is satisfied, thus a stable plateau (flat) region would have been reached. In order to ensure a linear response from the detector, the voltages for anode and grid must be chosen such that the detector operates in the plateau region. The avalanche region was not reached because there were insufficient free electrons with enough energies to break down the covalent bonds of iso-butane gas atoms and consequently liberate some electrons from the covalent bonds. The inequality on the left (10.67) ≥ right (1.92) of Eq. (2.8) is satisfied with the recommended operating voltages that are given in Table 3.4.

Table 3.4: Recommended operating conditions for the ΔE gas-ionisation detector determined using iso-butane gas at a differential pressure of 1 kPa.

Iso-butane Differential pressure (kPa)	V_A **(V)**	V_G **(V)**	V_C **(V)**	$V_A - V_G$ **(V)**	$V_G - V_C$ **(V)**
1.00	230	30	-30	200	60

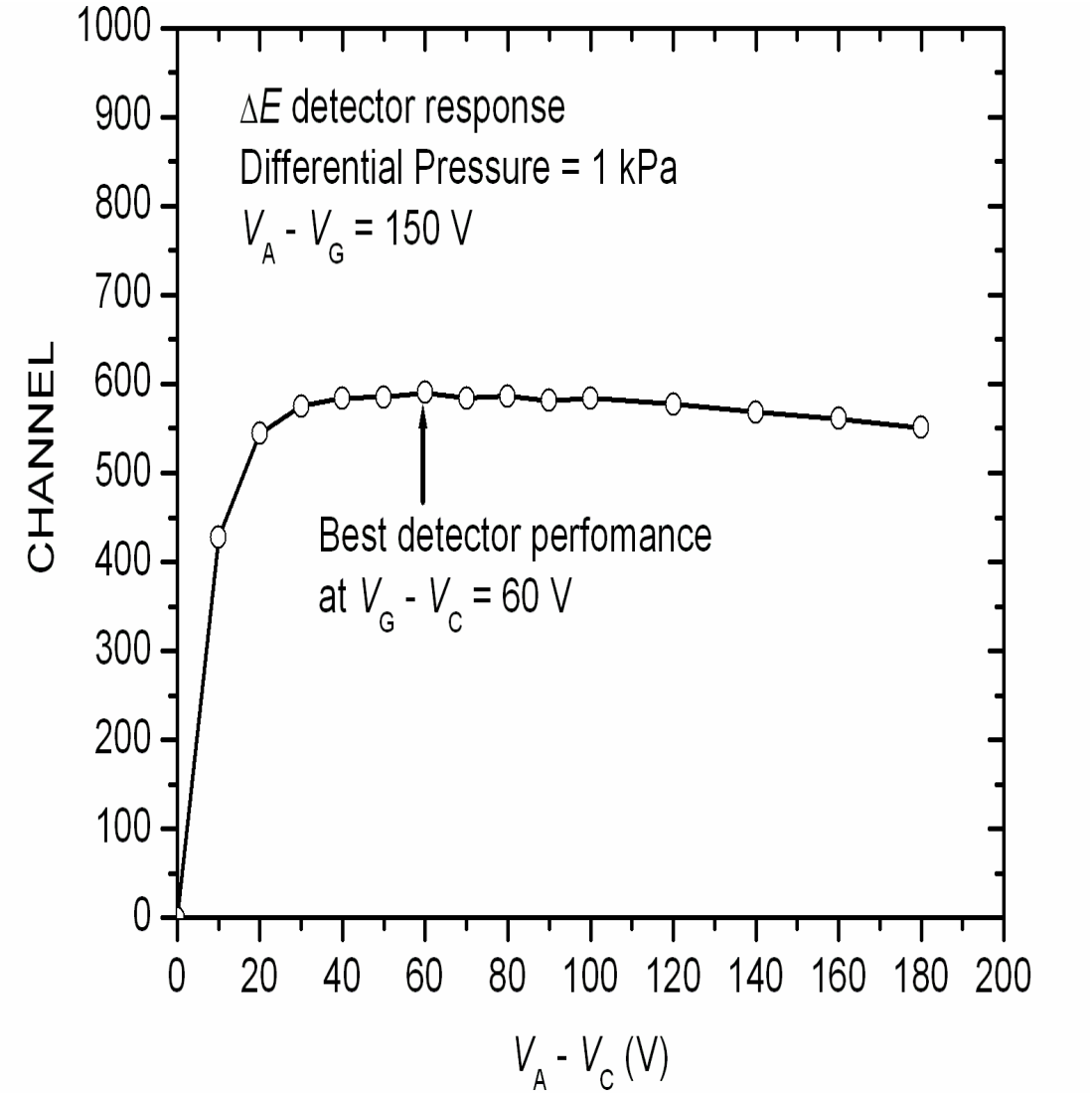

Figure 3.7: The dependence of the ΔE peak maximum on the potential difference between the grid and the cathode.

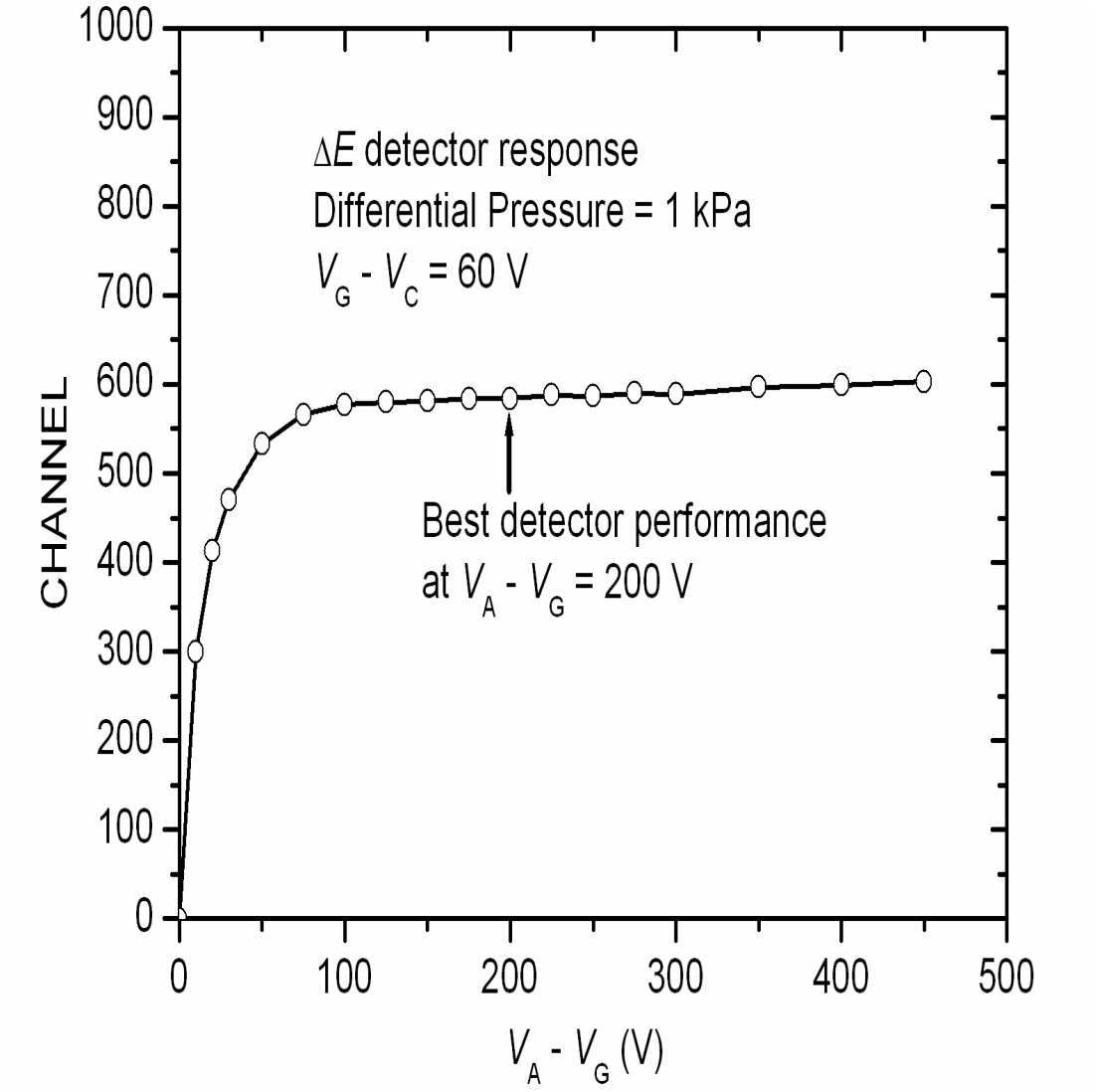

Figure 3.8: The dependence of the ΔE peak maximum on the potential difference between the anode and grid.

3.6 Heavy-ion scattering measurement using the ΔE-E gas-ionisation detector

The nature of the heavy-ion scattering process is determined mainly by the collision energy. The Coulomb barrier energy, $E_{\mathrm{Lab}}^{\mathrm{CB}}$, being defined as the energy required in a head-on collision for the two nuclear surfaces just to touch, thus for energies $E_{\mathrm{Lab}} \ll E_{\mathrm{Lab}}^{\mathrm{CB}}$, the interaction between the colliding nuclei happens via the long-range Coulomb field only, resulting in the classical Rutherford scattering [RU11] and inelastic scattering due to the Coulomb excitation [AL56]. In the case of energies $E_{\mathrm{Lab}} \approx E_{\mathrm{Lab}}^{\mathrm{CB}}$, effects of the short-range nuclear field start to become significant leading to a pronounced decrease in the Rutherford scattering cross-section that is observed at more backward scattering angles associated with close nuclear encounters. Therefore, the incident flux that would have gone into the elastic scattering channel thus tends to emerge in the increasing number of inelastic and reaction scattering channels that become available. It is in this energy region that the Coulomb and nuclear fields interfere strongly, resulting in a phenomenon known as Coulomb-nuclear interference [VI72].

The elastic scattering of ^{16}O from ^{28}Si was measured using the nuclear physics line (C-line) shown in Fig. 3.1. A heavy-ion beam of ^{16}O at an incident energy of 30.000 ± 0.038 MeV was scattered off an evaporated self-supporting SiO_2 target. The beam was focussed into the small scattering chamber and the high resolution ΔE-E gas-ionisation detector was used to detect the scattered particles. Heavy ion identification is based on the energy loss, ΔE, to ionisation of the molecules of a gas as it traverses the sensitive volume and the residual energy, E, deposited in a solid state surface-barrier detector at the end of the ΔE-E gas-ionisation detector. The principle of operation and the specifications of the ΔE-E gas-ionisation detector are discussed in Section 3.5. A computerised multi-channel on-line data acquisition system (CAMAC + WIMPS2 [FE92]) was used to identify the number, the energies and the types of particles emitted, by processing the ΔE and E signals of the detector. An angular distribution was measured in steps of θ_{Lab} = 2.5º between the angular range indicated in Table 3.5 at an incident energy just below the Coulomb barrier ($E_{\mathrm{Lab}}^{\mathrm{CB}}$(^{16}O + ^{28}Si) = 32.6 MeV).

Table 3.5: Scattering angles covered in ^{16}O + ^{28}Si elastic-scattering measurements.

E_{Lab} **(MeV)**	**Reaction Products**	**Nucleus detected**	θ_{Lab}	$\theta_{c.m.}$
30.000 ± 0.038	^{16}O (g.s)+ ^{28}Si (g.s)	^{16}O	15.5° - 70.5°	24.3°- 103.0°

Since the *Coulomb barrier energy* is defined as the energy due to the electrostatic interaction that two nuclei need to overcome so they can get close enough to undergo nuclear fusion, therefore the parameters that were used to calculate the Coulomb barrier are given in Table 3.6.

Table 3.6: Parameters that were used to calculate the Coulomb barrier energy.

E_{Lab}^{CB} (MeV)	Z_1 (Projectile-atomic number)	Z_2 (Target-atomic number)	A_1 (Projectile-mass number)	A_2 (Target-mass number)	r_0 (interaction radius/ **fm**)
32.6	8	14	16	28	1.4

The Coulomb barrier energy in both *laboratory* and *centre-of-mass* reference frames was calculated using the following equations respectively:

$$E_{\text{Lab}}^{\text{CB}} = E_{\text{c.m.}}^{\text{CB}}\left[\frac{A_1 + A_2}{A_2}\right], \tag{3.3a}$$

$$E_{\text{c.m.}}^{\text{CB}} = \frac{Z_1 Z_2 e^2}{r_0(A_1^{1/3} + A_2^{1/3})}. \tag{3.3b}$$

Furthermore, absolute normalisation of the measured scattering cross-sections was achieved by assuming the elastic scattering at the most forward angles to be purely Rutherford scattering.

3.6.1 Beam production and transportation

The ion source used was a model 860 A caesium sputter negative ion source which produced the negative ion beams of $^{16}O^-$. The copper cathode contained material used to make a sputtering target of 40% aluminium oxide and 60% copper powder. After mass analysis by means of the inflection magnet and collimation by means of X-Y slits, the $^{16}O^-$ beam was measured on the first Faraday cup before it was steered, focussed and transported to the injection point in front of the EN Tandem accelerator. Good beam alignment was accomplished with the aid of the last two beam profile monitors on the injection line. Beam transportation was fairly easy up to the last Faraday cup of the high-energy beam line. The analysing magnet was then used to select the $^{16}O^{5+}$ charge state from the mixed charge state beam. The $^{16}O^{5+}$ beam was transported to the C-line via the switching magnet. Table 3.7 presents the parameters that were used to obtain the above mentioned beam.

Table 3.7: Parameters that were used to produce an $^{16}O^{5+}$ beam of 30.000 ± 0.038 MeV.

Beam Type	Charge	Terminal Voltage (MV)	NMR Frequency (MHz)	Hall Probe Voltage (mV)	Magnetic Field (kG)
^{16}O	5+	5.028	40.544	91.137	9.470

3.7 Data Acquisition System

Figure 3.9 shows the block diagram of the electronics arrangement used. The amplified unipolar outputs are fed into Analog-to-Digital Converters (ADCs) with a time lag of 2 μs with respect to the start of the strobe signal 14 μs wide, while bipolar outputs of the spectroscopic amplifiers were used for timing and identification purposes.

The amplified bipolar outputs from the monitor and *E* detector were fed into the Timing Single Channel Analysers (TSCA's) and the three unipolar outputs were brought into coincidence with each other by the use of delay amplifiers. One of the two bipolar signals inputted to a logic OR gate was used to generate a strobe signal and then the remaining logic signal was processed by a pattern gate in coincidence with a channel zero signal that was a non Δ*E*-*E* event.

The gate, Δ*E*, *E* and Monitor digitised signals were brought into time coincidence for processing through the use of the Analog-to-Digital Converters of the CAMAC system. The converted signals from the CAMAC system were obtained through the use of WIMPS OS/2 computer programme [FE92] for all on-line data extraction and analysis. The signal of Δ*E* was plotted against E_T, where $E_T = (E_{stop} + n\Delta E)$ is the total kinetic energy and *n* is a factor used to normalise the Δ*E* signal to the *E* signal. In order to determine a value for the factor *n*, the position of the elastic scattering peak of interest in the energy spectrum obtained with the E_{stop} detector is obtained with the Δ*E* ionisation chamber GAS OFF and then with GAS ON. The elastically scattered peak is thus moved down in the energy spectrum due to energy loss in the Δ*E* detector with the GAS ON. In order to move the peak back to its original position with GAS OFF for a Δ*E* versus $E_T = E_{stop} + n\Delta E$ plot the factor *n* is determined ($n = 0.3865$) to multiply the corresponding Δ*E* peak position by.

A monitor detector positioned at a forward angle of 45º was used to check on the state of the evaporated self-supporting SiO_2 target and for beam current integration since it is more reliable than a beam current integrator which is sensitive to fluctuations in average charge state of the beam [VI93]. An example of a two dimensional Δ*E* versus E_T plot is shown in Fig. 3.10.

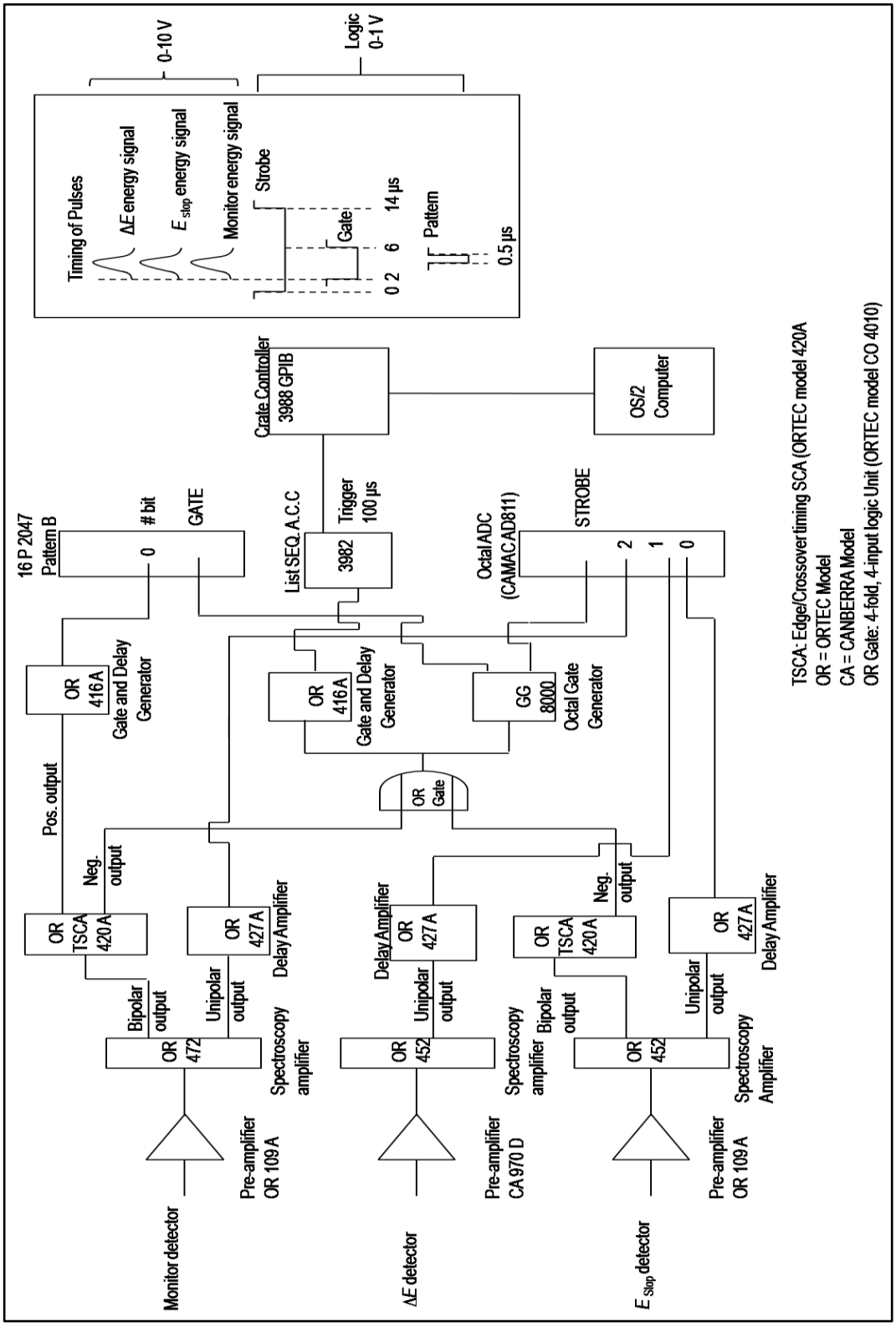

Figure 3.9: Block diagram of the electronics associated with the Δ*E*-*E* gas-ionisation detector.

Chapter 4

Measurement of ^{16}O + ^{28}Si elastic scattering: data extraction, analysis and discussion

This chapter presents a detailed description of the data extraction procedures that were followed and the determination of the elastic scattering cross-sections. Finally, the analysis of the scattering cross-sections using the optical model prediction is given.

4.1 ^{16}O + ^{28}Si elastic scattering: data extraction

By way of example, Fig. 3.11 shows the projection of the ^{16}O locus in the two-dimensional ΔE-E_T spectrum of ^{16}O on ^{28}Si at E_{Lab} = 30.000 ± 0.038 MeV at θ_{Lab} = 20.5° as shown in Fig. 3.10. Peaks of interest identified in the respective ^{16}O projections were fitted using a least squares technique with a Gaussian function and quadratic background.

Thus the formula used to fit peaks in the measured spectra may be written as:

$$y(x) = h\exp\left\{-\frac{1}{2}\left(\frac{x-x_0}{\sigma}\right)^2\right\} + c_0 + c_1x + c_2x^2, \tag{3.4}$$

where x_0 is the centroid, h is the height of the peak, σ is the standard deviation, x is the channel number and the constants c_1, c_2, and c_3 define the quadratic background. Hence, the area under the Gaussian can be obtained from

$$A = h\sigma\sqrt{(2\pi)}, \tag{3.5}$$

and the total area under the peak is given by

$$P = A + b, \tag{3.6}$$

where A is the peak area and b is the background under the peak.

Peaks of the one-dimensional ΔE-E_T spectrum resulting from elastic scattering were extracted by computer fitting using Eq. (3.4), except for a few instances when the yield was low. The uncertainty, ΔA, of the extracted peak is given by

$$\Delta \mathrm{A} = \left[(P+b)\chi^2 \right]^{\frac{1}{2}} = \left[(A+2b)\chi^2 \right]^{\frac{1}{2}}, \tag{3.7}$$

where χ^2 is referred as the minimum reduced chi-squared parameter and is defined as

$$\chi^2 = \frac{1}{N} \sum_i \left[\frac{y_i - y(x_i)}{(y_i)^{\frac{1}{2}}} \right]^2, \tag{3.8}$$

with N the number of degrees of freedom (number of data points minus the number of variable parameters) and $(y_i)^{\frac{1}{2}}$ are the uncertainties on the data points y_i [CA78].

Absolute normalisation of the cross-section was achieved by normalising the angular distributions experimental data to the theoretical prediction according to the optical model calculations.

4.1.1 Energy resolution of the detector system

The term '*Energy Resolution*' is generally defined as the extent to which a detector can distinguish two close lying peaks. In addition to the fluctuations in ionisation, a number of external factors can affect the overall resolution of a ΔE-E_T gas-ionisation detector. These include effects from the associated electronics such as noise, drifts, etc. Assuming all these sources are independent and distributed as Gaussians, the total energy resolution of the ΔE-E_T gas-ionisation detector can be written as:

$$\Delta E_{\mathrm{total}} = \left[(\Delta E_{\mathrm{kin}})^2 + (\Delta E_{\mathrm{loss}})^2 + (\Delta E_{\mathrm{det}})^2 + (\Delta E_{\mathrm{beam}})^2 \right]^{1/2}, \tag{3.9}$$

where the different components may be identified as

WIMPS\ $^{16}O + {}^{28}Si$ at E_{Lab} = 30.000 ± 0.038 MeV

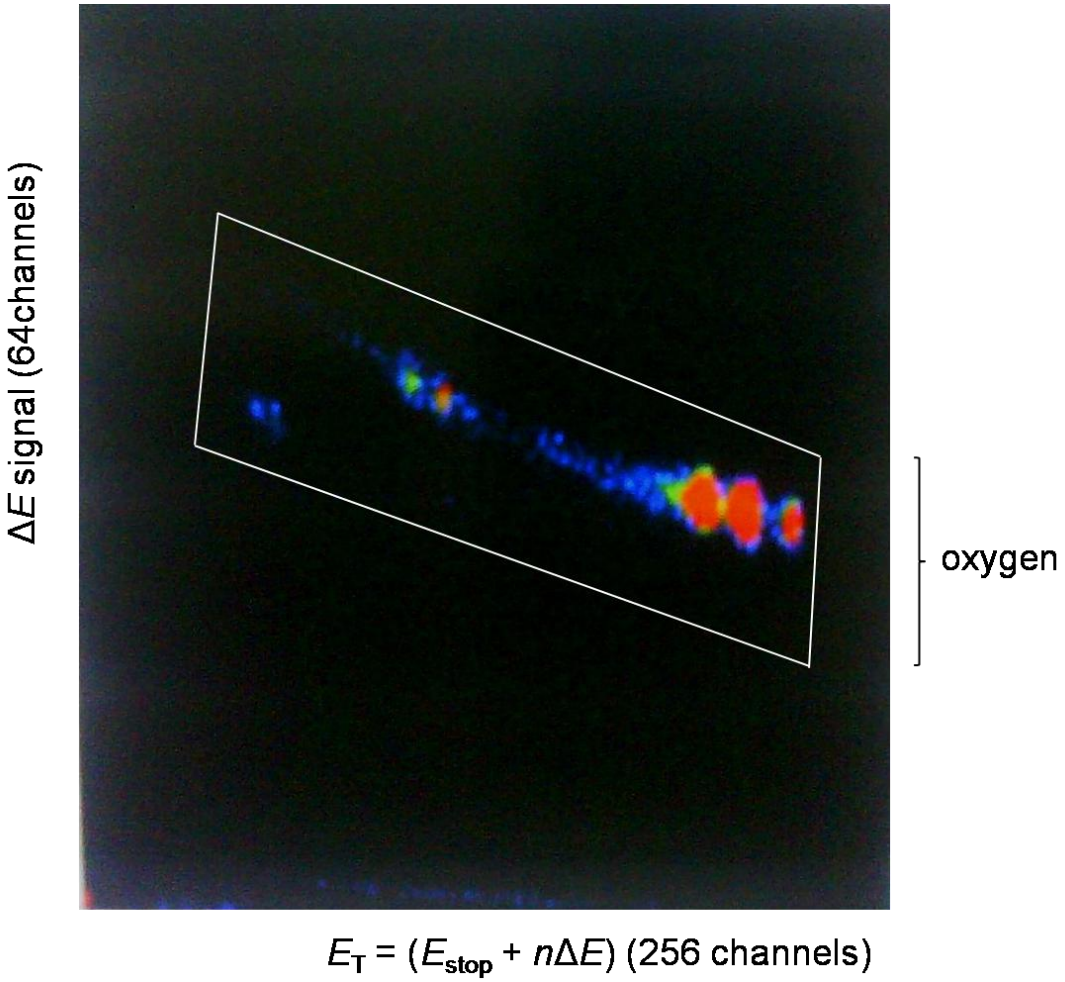

Figure 3.10: Two-dimensional ΔE-E_T spectrum of ^{16}O on ^{28}Si at E_{Lab} = 30.000 ± 0.038 MeV ($E_{c.m.}$ = 19.1 MeV) and θ_{Lab} = 20.5°.

- Kinematic broadening, ΔE_{kin}, related to the finite angular acceptance of the detector and divergence of the beam. It can be estimated to be approximately ≈ (190 keV/20.5º) = 9.27 keV/deg, at a scattering angle of 20.5º;
- Uncertainty of the energy loss, ΔE_{loss}, is due to the small-angle scattering and energy-loss straggling in the target and the thin window (≈100 keV);
- Detector resolution (electronic noise), ΔE_{det}, is the contribution from the resolution of the solid state surface-barrier detector and the electronics of the system (≈24 keV) and;
- Energy spread of the incident beam, ΔE_{beam}, was estimated to be approximately ≈10 keV.

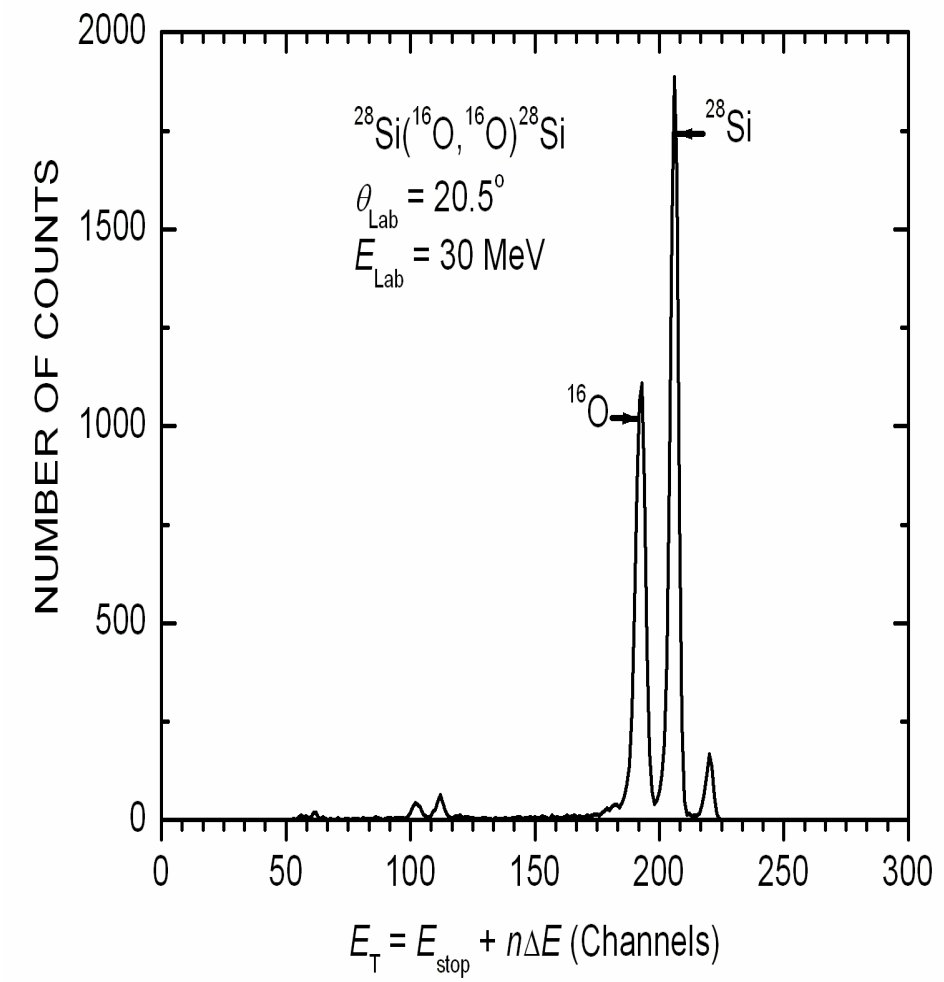

Figure 3.11: One-dimensional ΔE-E_T spectrum of ^{16}O on ^{28}Si at E_{Lab} = 30.000 ± 0.038 MeV ($E_{c.m.}$ = 19.1 MeV) and θ_{Lab} = 20.5°.

4.1.2 Treatment of Errors

Equation (3.7) was used for determining the uncertainty on the extracted yields. The uncertainties in the final results for elastic cross-sections obtained can be assumed to originate from the following sources:

(a) peak extraction uncertainties and,

(b) a normalisation uncertainty, taken to be the uncertainty in extracting the elastic peak area of the monitor.

4.2 Determination of scattering cross-sections

In order to determine elastic scattering cross-sections, the areas of the peaks of interest were extracted from the one-dimensional ^{16}O spectrum for each scattering angle (see Section 4.1). Absolute normalisation of the cross sections was achieved by assuming the elastic scattering at the most forward scattering angles to be purely Rutherford scattering. The following procedure was used to determine the elastic scattering cross-sections. Firstly, the elastic scattering yields of the scattered ^{16}O beam were referenced to a monitor detector placed at $\theta_{\mathrm{Lab}} = 45^{\circ}$ in order to normalise between runs. Secondly, the normalised laboratory yields were multiplied by the corresponding laboratory to centre-of-mass kinematic factors, in order to determine normalised centre-of-mass yields. Corresponding yields in the centre-of-mass reference frame $I(\theta_{\mathrm{c.m.}})$ were obtained using [MA68]

$$I(\theta_{\mathrm{c.m.}}) = I(\theta_{\mathrm{Lab}}) \left[\frac{\sin^2 \theta_{\mathrm{Lab}}}{\sin^2 \theta_{\mathrm{c.m.}}} \right] \cos(\theta_{\mathrm{c.m.}} - \theta_{\mathrm{Lab}}), \tag{3.10}$$

where $\theta_{\mathrm{c.m.}}$ is the centre-of-mass scattering angle and θ_{Lab} is the corresponding laboratory scattering angle.

Finally, the normalised centre-of-mass yields were then divided by the corresponding Rutherford scattering cross-sections in the centre-of-mass. The resulting $d\sigma/d\sigma_{\mathrm{Ruth}}$ should have a value of one at the most forward scattering angles which, in the present case, are purely due to Rutherford scattering.

4.3 Analysis for elastic scattering of ^{16}O + ^{28}Si

An elastic scattering angular-distribution for the ^{16}O + ^{28}Si system has been measured at an incident energy just below the Coulomb barrier (E_{Lab} = 30.000 ± 0.038 MeV, $E_{\mathrm{Lab}}^{\mathrm{CB}}$ = 32.6 MeV). The angular range covered is limited to the region $24.3^{\circ} \leq \theta_{\mathrm{c.m.}} \leq 103.0^{\circ}$. The experimental results for the present data and the theoretical prediction are shown in Fig. 3.12. The present results are also supplemented for comparison reasons with data set from a previous experiment of the same scattering reaction at an incident energy, E_{Lab} = 32 MeV [CA78].

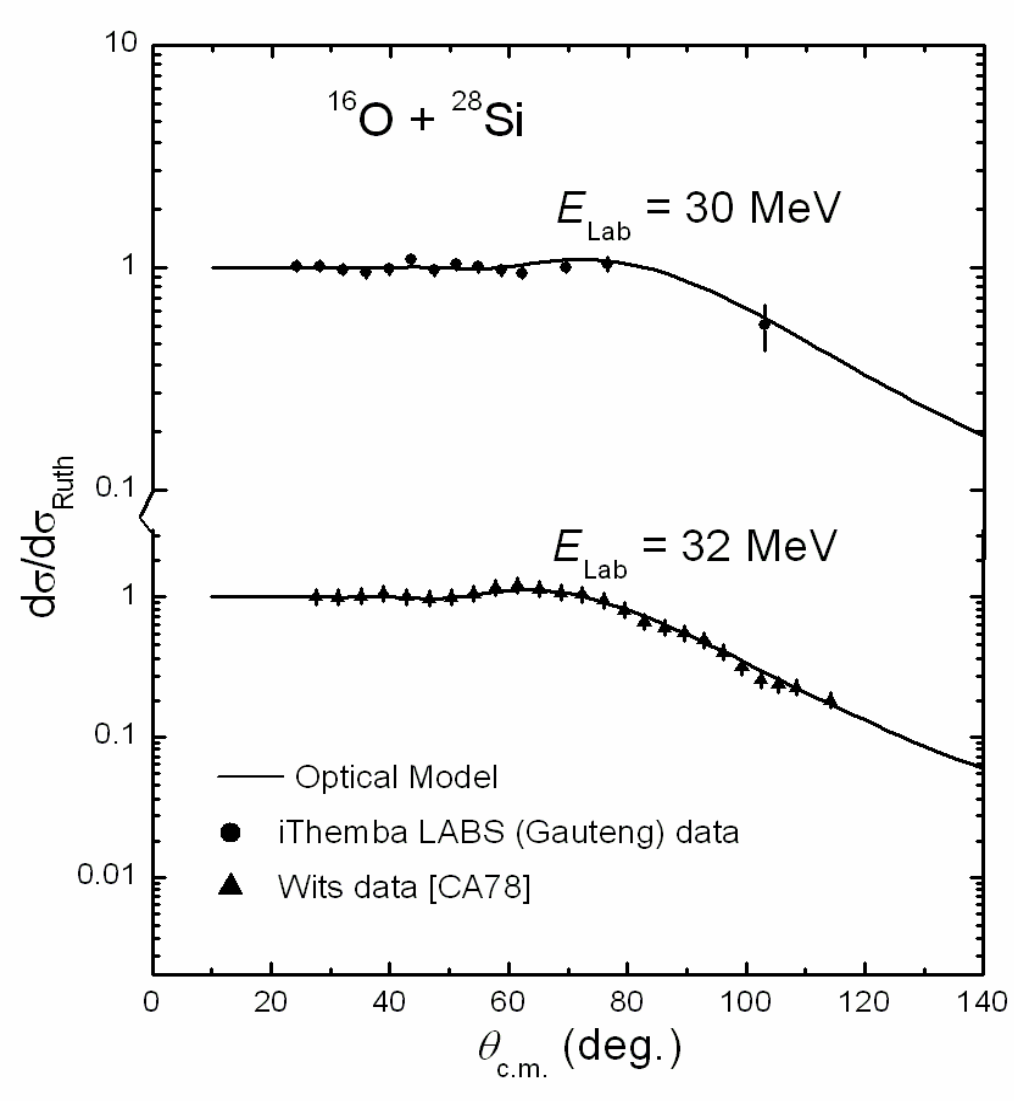

Figure 3.12: Angular distributions for elastic scattering of ^{16}O + ^{28}Si at E_{Lab} = 30.000 ± 0.038 MeV and 32 MeV. The 32 MeV data are from Carter [CA78].

Both sets of data show a similar and consistent trend. More specifically, both sets exhibit a ratio of $d\sigma/d\sigma_{Ruth}$ very close to one for the forward angle scattering between $\theta_{c.m.}$ = 20º to 60º, indicating a pure Rutherford elastic scattering. For centre-of-mass angles between $\theta_{c.m.}$= 60º and 80º, the data are seen to display a rise above the Rutherford cross-section as expected due to the constructive interference between the Coulomb and nuclear potentials. Finally, for centre-of-mass angles greater than $\theta_{c.m.}$ = 80º, the data are seen to be less than the Rutherford cross-section due to absorption effects.

In the present study, only one data point could be obtained for $\theta_{\text{c.m.}} > 80^{\circ}$, due to instabilities of the central terminal voltage of the EN Tandem accelerator at the time of measurement. This was due to a failure of the pumping system of the gas stripper placed in the centre terminal.

4.4 Optical model analysis for $^{16}O + ^{28}Si$

Elastic scattering cross-sections were calculated using the optical model prediction as described in Section 2.2.3. The optical model based calculations were performed using a modified version of Code *A-THREE* of Auerbach [AU78]. The interaction potential consists of four terms as according to

$$V = V_{\text{re}}(r) + \text{i}V_{\text{im}}(r) + V_{\text{so}}(r)\boldsymbol{l}.\boldsymbol{\sigma} + V_{\text{Coul}}(r)$$

where the four parts $V_{\text{re}}, V_{\text{im}}, V_{\text{so}}, V_{\text{Coul}}$ are called the real, imaginary, spin-orbit, and Coulomb parts of the potential, respectively. For this particular study the term V_{so} in the above equation is zero which implies we have a spin-zero problem. The nuclear potential used is of the Woods-Saxon type. In this calculation, the non-relativistic Schrödinger equation, with a complex scattering potential, is solved numerically, partial wave by partial wave, in order to obtain the nuclear phase shifts, from which the elastic scattering cross-sections are calculated. The imaginary part of the interaction potential was taken to be one of the volume absorption.

4.4.1 Woods-Saxon Potential

The real and imaginary nuclear optical potentials used in the optical model calculations were of a Woods-Saxon form as shown in Section 2.2.3. Table 3.8 presents the optical potential parameters that were used in the present optical model calculations.

Table 3.8: Optical potential parameters used in the optical model calculations [CA78].

Scattering Reaction	V_0 (MeV)	W_0 (MeV)	$R_{0R} = R_{0I}$ (fm)	a_R (fm)	a_I (fm)
^{28}Si(^{16}O,^{16}O)	12.55	9.96	1.37	0.53	0.36

4.5 Discussion

A good agreement between the optical model prediction for the elastic scattering angular distribution of the ^{16}O + ^{28}Si system at E_{Lab} = 30.000 ± 0.038 and 32 MeV was achieved. Oscillations are observed in the elastic scattering data at angles greater than the angle of the rise above the Rutherford cross-sections, thereby exhibiting an excellent correspondence with the previously reported measurements of ^{16}O + ^{28}Si at E_{Lab} = 32 MeV [CA78]. However, the angular distribution fits for both E_{Lab} = 30.000 ± 0.038 and 32 MeV show a purely excellent Rutherford scattering trend for small scattering angles below $\theta_{c.m.} \approx 60^{o}$.

Unfortunately, only one data point is available for the angular distribution of ^{16}O + ^{28}Si at E_{Lab} = 30.000 ± 0.038 MeV for $\theta_{c.m.} \approx 80^{o}$ where nuclear absorption effects become important. However, since the aim of the measurement was to check if all components of the iThemba LABS (Gauteng) facility were working satisfactorily, therefore, it is gratifying to note that the measured data for $\theta_{c.m.} \approx 60^{o}$ consistently have a value close to one, as expected for pure Rutherford scattering.

Chapter 5

Conclusions

The plateau region of the ΔE part of a high resolution ΔE-E gas-ionisation detector was determined and further confirmed by the use of Eq. (2.8) in Section 2.1. The consistency in Figs. 2.2, 3.7 and 3.8 is a strong argument which confirms that an increase in the ratio of the field strengths given by the left side of Eq. (2.8) allows the establishment of the plateau region. The multiple series of discrete peaks from the one dimensional spectrum of ^{16}O on ^{28}Si in Section 4.1, is a strong evidence that enables the ΔE-E gas-ionisation detector to be reliably used for different particle identification purposes,

The striking similarity between the observed angular distribution at E_{Lab} = 30.000 ± 0.038 MeV and the theoretical optical model prediction, especially in the precipitous fall in the region $\theta_{\text{c.m.}}$ = 80º to 100º, indicates the success of the didactic exercise that was performed, since the experimental scattering data and the theoretical calculated data agreed relatively well, thereby confirming that the newly refurbished EN Tandem accelerator of iThemba LABS (Gauteng), the nuclear structure beam line (C-line) and the ΔE-E gas-ionisation chamber with its associated electronics and data acquisition system have been successfully commissioned and are ready for use in further nuclear structure studies.

Furthermore, the good correspondence (consistency) of the two fits for angular distribution data at E_{Lab} = 30.000 ± 0.038 and 32 MeV [CA78] is another excellent confirmation which highlights that the ΔE-E gas-ionisation detector was accurately calibrated. Finally, the results of the present analysis show that the elastic-scattering data obtained from ^{16}O + ^{28}Si reaction at E_{Lab} = 30.000 ± 0.038 MeV, was measured as purely Rutherford scattering for $\theta_{\text{c.m.}} \leq 60^{\text{o}}$.

Bibliography

[AD06] S. Adhikari, C. Basu, C. Samanta, S. S. Brahmachari, B. P. Das, and P. Basu, *Perfomance of an axial gas ionisation detector*, IEE Transactions on Nuclear Science, vol. 53, no. 4 (2006) 2270 - 2275.

[AL56] K. Alder, A. Bohr, T. Huus, B. Mottelson and A. Winther, Rev. Mod. Phys. 28 (1956) 432.

[AU78] E. H. Auerbach, A-Three: *A general optical model code especially suited to heavy-ion calculations*, Computer Physics Communications 15 (1978) 165-192.

[BA75] J. Barrete, P. Braun-Munzinger and C. K. Gelbke, Nucl. Instr. and Meth. 126 (1975) 181.

[BU46] O. Bunemann, Nuclear Research Council Report (1946) 285.

[BE64] Sergio DeBenedetti, *Nuclear interactions* (John Wiley & Sons Inc. 1964) 74.

[CA78] J. M. Carter, *Inelastic scattering of heavy ions from light nuclei at energies near the coulomb barrier*, Doctor of Philosophy, University of the Witwatersrand, (1978).

[CA81] B. O. Carragher, *Heavy ion α-transfer reactions*, MSc Dissertation, University of the Witwatersrand, (1981).

[FE54] H. Feshbach, C. E. Porter and V. F. Weisskopf, Phys. Rev. 96 (1954) 488.

[FE92] R. W. Fearick, WIMPS 2 *multi-parameter data acquisition system* OS/2, Computer Programme (1992).

[GO64] F. S. Goulding, D. A. Landis, J. Cerny and R. H. Pehl, Nucl. Instr. and Meth. 31 (1964) 2.

[GO79] F. S. Goulding, Nucl. Instr. and Meth. 162 (1979) 609.

[GL57] A. E. Glassgold and P. J. Kellogg, Phys. Rev. 107 (1957) 1372.

[GL83] N. K. Glendenning, *Direct Nuclear reactions*, World Scientific, 5 Toh Tuck Link, Singapore (1983).

[JA70] D. F. Jackson, in *Nuclear Reactions* (Methuen, London, 1970) C - p. 124, D - p. 121.

[JA83] A. N. James, P. A. Butler, T. P. Morrison, J. Simpson, and K. A. Connell, "*The response of an isobutane filled ion chamber to heavy ions*", Nucl. Instr. And Meth. Vol. 212 (1983) 545 - 553.

[JI08] M. Jingo, C. O. Kureba, J. Carter and E. Sideras-Haddad, *Nuclear Structure studies at the 6 MV EN Tandem accelerator of iThemba LABS (Gauteng)* SAIP Conference (2008).

[KR88] Kenneth S. Krane, *Introductory Nuclear Physics*, (John Wiley & sons, New York, 1988) 396-405.

[LA07] Kobus Lawrie, iThemba LABS Editor (South Africa, 2007) http://www.tlabs.ac.za.

[LA07] A. Larson, J. B. Roos, M. Stenrup and A. E. Orel, *ion pair formation in electron recombination with molecular ions*, Journal of Physics: Conference Series **88** (2007) 012065. http://iopscience.iop.org/1742-6596/88/1/012065.

[LE87] W. R. Leo, *Techniques for Nuclear and Particle Physics Experiments* (Springer-Verlag Berlin Heidelberg, 1987) 124.

[LE92] W. R. Leo, *Techniques for Nuclear and Particle Physics Experiments* (Springer, Berlin Heidelberg New York, 1992).

[LI37] M. S. Livingston and H. A. Bethe, Rev. Mod. Phys. 9 (1937) 261.

[MA68] J. B. Marion and F. C. Young, *Nuclear Reactions Analysis* (North-Holland-Amsterdam, 1968) 39-41, 140-142.

[ME58] A. Messiah, *Quantum Mechanics*, (John Wiley and sons, New York, 1958) 412.

[OE75] W. Von Oertzen and H. G. Bohlen, *Elastic transfer processes in Heavy ion scattering*, Phys. Rep. 19 (1975) 1-61.

[RU11] E. Rutherford, Phil. Mag.21 (1911) 669.

[VI72] F. Videbaek, I. Chernov, P. R. Christensen and E. E. Gross, Phys. Rev. Lett. 28 (1972) 1072.

[VI93] Zeblon Zenzele Vilakazi, *Cluster transfers between ^{9}Be and ^{12}C leading to bound and unbound states in the same system*, MSc Dissertation, University of the Witwatersrand, (1993).

[WO54] R. D. Woods and D. S. Saxon, Phys. Rev. 95 (1954) 577.

[WI50] D. H. Wilkinson, *Ionization Chambers and Counters*, (Cambridge univ. Press. 1950). A-p74, B-p77.

Appendix

Tabulated values of the measured Quantities

Table A1: Values for the inflection magnet and low energy cup currents.

Inflection magnet current/A	Low energy cup current/nA	Inflection magnet current/A	Low energy cup current/nA	Inflection magnet current/A	Low energy cup current/nA
0.00	0	5.60	0	13.42	3597
1.00	0	6.50	0	13.48	3762
2.00	0	7.00	0	13.51	4055
3.30	0	8.00	0	13.52	4109
3.32	13	8.50	0	13.55	4187
3.41	27	9.00	0	13.59	4198
3.36	44	10.00	0	13.63	4249
3.38	62	11.00	0	13.70	4280
3.41	78	12.00	0	13.73	4255
3.44	108	12.50	0	13.79	4176
3.45	109	12.80	0	13.80	4015
3.46	110	12.82	0	13.81	4007
3.47	110	12.84	7	13.86	3802
3.48	110	12.87	27	13.90	3690
3.49	111	12.90	82	13.91	3395
3.50	110	12.94	157	14.00	3273
3.51	109	12.98	295	14.10	2578
3.52	108	13.02	500	14.20	1744
3.54	102	13.04	739	14.30	874
3.56	89	13.07	877	14.32	426
3.58	66	13.10	1095	14.40	191
3.61	46	13.13	1332	14.50	182
3.66	1	13.17	1567	14.60	131
3.70	0	13.20	1919	14.70	91
3.80	0	13.24	2242	14.80	61
4.00	0	13.27	2505	14.90	28
4.50	0	13.31	2444	15.00	1
5.00	0	13.35	3057	15.10	0
5.50	0	13.39	3336	15.20	3

Inflection magnet current/A	Low energy cup current/nA	Inflection magnet current/A	Low energy cup current/nA	Inflection magnet current/A	Low energy cup current/nA
15.3	16	18.2	29	21.4	0
15.4	31	18.3	128	21.6	0
15.5	46	18.5	300	21.8	0
15.6	60	18.6	512	21.9	0
15.7	73	18.7	740	22.0	0
15.8	82	18.8	957	22.2	0
15.9	81	18.9	157	22.4	0
16.0	75	19.0	1380	22.5	0
16.1	64	19.1	1488	22.6	22
16.2	51	19.2	1576	22.7	40
16.3	36	19.3	1602	22.8	55
16.4	25	19.4	1617	22.9	70
16.5	16	19.5	1598	23.0	83
16.6	17	19.6	1501	23.1	96
16.7	25	19.7	1349	23.2	106
16.8	32	19.8	1125	23.3	114
16.9	41	19.9	875	23.4	117
17.0	42	20.0	434	23.5	118
17.1	45	20.2	248	23.6	118
17.2	44	20.3	142	23.7	118
17.3	43	20.4	71	23.8	115
17.4	37	20.5	36	23.9	107
17.5	30	20.6	20	24.0	93
17.6	21	20.7	4	24.1	79
17.7	12	20.8	0	24.2	56
17.8	3	20.9	0	24.3	42
17.9	0	21.0	0	24.4	27
18.0	0	21.1	0	24.5	14
18.1	0	21.2	0	24.6	2

Inflection magnet current/A	Low energy cup current/nA	Inflection magnet current/A	Low energy cup current/nA	Inflection magnet current/A	Low energy cup current/nA
24.7	0	27.9	0	31.9	0
24.8	0	28.0	0	32.0	3
24.9	0	28.2	0	32.1	3
25.0	0	28.4	0	32.2	4
25.1	0	28.6	0	32.3	5
25.2	0	28.8	0	32.4	5
25.3	0	29.0	0	32.8	5
25.4	0	29.2	0	32.9	5
25.5	0	29.4	0	33.0	5
25.6	0	29.6	0	33.2	5
25.7	2	29.9	0	33.3	5
25.8	13	30.0	0	33.4	2
26.0	24	30.1	0	33.5	0
26.2	37	30.2	0	33.6	0
26.3	49	30.3	2	34.0	0
26.4	59	30.4	3	34.2	0
26.5	77	30.5	5	34.5	0
26.6	83	30.6	6	34.9	0
26.7	88	30.7	7	35.0	0
26.8	90	30.8	8	35.2	0
26.9	91	30.9	8	35.3	0
27.0	91	31.0	7	36.0	0
27.2	89	31.1	7	39.0	0
27.3	87	31.2	6	40.0	0
27.4	86	31.3	4		
27.5	86	31.4	3		
27.6	48	31.5	2		
27.7	25	31.6	1		
27.8	5	31.8	0		

Table A2: ΔE peak maximum values for constant $V_A - V_G = 150$ V and variation of $V_G - V_C$.

V_A (V)	V_G (V)	V_C (V)	$V_A - V_G$ (V)	$V_G - V_C$ (V)	ΔE peak maximum (Channel)
150	00	00	150	00	000
155	5	-5	150	10	428
160	10	-10	150	20	544
165	15	-15	150	30	575
170	20	-20	150	40	584
175	25	-25	150	50	585
180	30	-30	150	60	590
185	35	-35	150	70	584
190	40	-40	150	80	586
195	45	-45	150	90	581
200	50	-50	150	100	584
210	60	-60	150	120	577
220	70	-70	150	140	568
230	80	-80	150	160	561
240	90	-90	150	180	551

Table A3: ΔE peak maximum values for constant $V_G - V_C = 60$ V and variation of $V_A - V_G$.

V_A (V)	V_G (V)	V_C (V)	V_A - V_G (V)	V_G - V_C (V)	ΔE peak Maximum (Channel)
30	30	-30	00	60	000
40	30	-30	10	60	300
50	30	-30	20	60	413
60	30	-30	30	60	470
80	30	-30	50	60	533
105	30	-30	75	60	566
130	30	-30	100	60	577
155	30	-30	125	60	580
180	30	-30	150	60	581
205	30	-30	175	60	584
230	30	-30	200	60	584
255	30	-30	225	60	588
280	30	-30	250	60	587
305	30	-30	275	60	590
330	30	-30	300	60	589
380	30	-30	350	60	597
430	30	-30	400	60	599
480	30	-30	450	60	603

Table A4: Elastic scattering of $^{16}O + ^{28}Si$ at E_{Lab} = 30.000 ± 0.038 MeV.

$\theta_{c.m.}$ (deg.)	$d\sigma / d\sigma_R$	Error
24.28	1.014	0.018
28.17	1.012	0.020
32.04	0.974	0.014
35.9	0.945	0.017
39.74	0.979	0.018
43.56	1.084	0.023
47.36	0.972	0.019
51.13	1.034	0.016
54.88	1.005	0.016
58.6	0.972	0.019
62.28	0.939	0.014
69.55	1.003	0.035
76.66	1.035	0.073
103.09	0.548	0.128

Table A5: Elastic scattering of $^{16}O + ^{28}Si$ at E_{Lab} = 32 MeV [CA78].

$\theta_{c.m.}$	$d\sigma / d\sigma_R$	**Error**
27.48	0.998	0.020
31.27	0.995	0.028
35.13	1.008	0.040
38.98	1.052	0.032
42.8	1.001	0.032
46.6	0.973	0.032
50.38	0.989	0.030
54.13	1.050	0.029
57.86	1.159	0.034
61.55	1.203	0.035
65.21	1.131	0.035
68.83	1.069	0.027
72.42	1.040	0.029
75.96	0.943	0.028
79.46	0.799	0.022
82.91	0.663	0.017
86.31	0.603	0.012
89.66	0.549	0.012
92.96	0.491	0.008
96.19	0.401	0.007
99.37	0.316	0.003
102.48	0.255	0.005
105.52	0.236	0.004
108.50	0.226	0.003
114.25	0.183	0.010